Fe-modified Mn2CuO4 spinel oxides: coatings based on abundant elements for solid oxide cell interconnects

Available online at www.sciencedirect.com

ScienceDirect

journal homepage: www.elsevier.com/locate/he

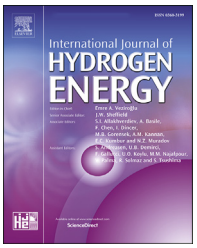

Fe-modified Mn_2CuO_4 spinel oxides: coatings based on abundant elements for solid oxide cell interconnects

Justyna Ignaczak [a,*], *Lunjie Zeng* [b], *Dario Ferreira Sanchez* [c], *Małgorzata Makowska* [d], *Karolina Górnicka* [e], *Krystian Lankauf* [a], *Jakub Karczewski* [e], *Piotr Jasiński* [a], *Sebastian Molin* [a]

[a] *Advanced Materials Center, Faculty of Electronics, Telecommunications and Informatics, Gdańsk University of Technology, ul. G. Narutowicza 11/12, 80-233 Gdańsk, Poland*

[b] *Department of Physics, Chalmers University of Technology, 412 96 Gothenburg, Sweden*

[c] *MicroXAS Beamline, Paul Scherrer Institut, Forschungsstrasse 111, Villigen PSI, 5232 Switzerland*

[d] *Photons for Engineering and Manufacturing, Paul Scherrer Institut, Forschungsstrasse 111, Villigen PSI, 5232 Switzerland*

[e] *Advanced Materials Center, Faculty of Applied Physics and Mathematics, Gdańsk University of Technology, ul. G. Narutowicza 11/12, 80-233 Gdańsk, Poland*

HIGHLIGHTS

- $MnCo_2O_4$, Mn_2CuO_4, $Mn_{1.9}CuFe_{0.1}O_4$, $Mn_{1.7}CuFe_{0.3}O_4$ were synthesized via a sol-gel method and compared as a coating material.
- The effect of Fe addition on structural and protective properties was investigated.
- Synchrotron multimodal chemical imaging allowed the phase composition to be identified.
- ASR of $Mn_{1.7}CuFe_{0.3}O_4$ coated steel after 3000 h of oxidation was excellent.

ARTICLE INFO

Article history:
Received 13 April 2023
Received in revised form
31 May 2023
Accepted 4 June 2023
Available online xxx

ABSTRACT

The current state of the art steel interconnect coating materials are based on critical raw material - Co-oxide spinels. Replacing Co-oxide spinels with alternative, abundant materials can reduce the dependence on the critical raw materials. Cobalt-free coatings with the general formula $Mn_{2-x}CuFe_xO_4$, where x = 0, 0.1, 0.3, were electrophoretically deposited on a ferritic stainless-steel support and evaluated. Prior to deposition, the powders were prepared by a soft chemistry process and studied in terms of crystallographic phase analysis, electrical conductivity, thermal expansion, and sinterability behaviour. Coated steel samples were oxidised in an air atmosphere at 750 °C for 3000 h. In parallel, a state-of-the-art $MnCo_2O_4$ spinel oxide was tested as a reference. The coatings and oxide scale microstructures of the surfaces and cross-sections were examined by XRD, and SEM-EDX. TEM-EDX, XRF, and micro-XRD were also performed on the cross-section lamellae. The electrical properties of the steel-coating system were evaluated by Area Specific Resistance measurement. The results confirm that Mn–Cu–Fe oxides exhibit higher conductivity and

* *Corresponding author.*
E-mail address: justyna.ignaczak@pg.edu.pl (J. Ignaczak).

https://doi.org/10.1016/j.ijhydene.2023.06.041

lower TEC than Mn–Co oxide. Based on the obtained results, it might be concluded that the proposed coatings are a promising alternative to coatings that contain cobalt.

Introduction

The current energy market situation and the growing necessity to use renewable energy sources is the driving force behind the development of electrochemical energy conversion devices. Solid Oxide Cells (SOCs) can be used to convert fuels to electrical energy and to store electrical energy via electrolysis. There are, however, several factors limiting the large-scale introduction of these devices to industries. One of the main challenges is the degradation of the ferritic stainless steel (FSS) used as an interconnect material. At high operating temperatures, the FSS oxidises, forming a layer of corrosion products (depending on the elemental composition of the alloy, Cr_2O_3 and/or $(MnCr)_3O_4$) on the surface. These oxides have low electrical conductivity at high temperatures [1,2]. During cell operation, the oxide layer grows, further decreasing the conductivity and therefore leading to power losses. Furthermore, the chromium in the alloy evaporates from the surface, forming chromium compounds that cause oxygen electrode degradation also called cathode poisoning. Thus, protective coatings have been developed to slow down the oxidation of the steel and to stop the evaporation of chromium. The current state of the art coatings are typically made of $(Mn,Co)_3O_4$ spinel oxides. Researchers are currently focusing on improving the physicochemical properties (e.g. thermal expansion coefficient, electrical conductivity, etc.) of these layers by doping them with other elements, mainly with iron and copper [1–4] but there were also attempt to introduce into structure nickel and cerium [3,4]. However, due to the limited availability and rising cobalt prices, alternative coating materials are sought. Mn–Cu spinels show potential to solve problems caused by the current coatings, however, they have been described in only a few papers [5–10] and a detailed characterisation of these materials is still lacking.

In comparison to $(Mn,Co)_3O_4$ spinel oxides, $(Mn,Cu)_3O_4$ spinel oxides have a thermal expansion coefficient (TEC) better matched to ferritic stainless steel. They also have a higher electrical conductivity, are less expensive to produce, and are more environmentally friendly as they do not contain carcinogenic cobalt. The challenge with replacing cobalt with copper is that $(Mn,Cu)_3O_4$ spinel exhibits a lower phase stability. Sun et al. prepared a $Cu_{1.3}Mn_{1.7}O_4$ coating by electrophoretic deposition, in which, after sintering treatment, a CuO layer was formed on the coating surface [11]. Joshi and Petric successfully stabilised the spinel phase by adding nickel to $Cu_{1.18}Mn_{1.82}O_4$, which revealed a secondary, non-spinel, phase [6]. However, there have also been successful attempts to prepare a single-phase Mn–Cu spinel coating. For example, Huang successfully deposited $CuMn_{1.8}O_4$ spinel on Crofer 22 APU and obtained a dense spinel cubic phase coating [12].

In our previous work [13], we modified a manganese copper spinel by adding iron, and obtained stoichiometry: $Mn_{1.7}Cu_{1.3-x}Fe_xO_4$ where x = 0, 0.1, 0.3, 0.5. The powders were evaluated in terms of phase stability at high temperatures, and the research focused on the basic physico-chemistry of the powders and sintered pellets. Fe substituted Mn1.7Cu1.3-xFexO4 spinel-based ceramics (x = 0, 0.1, 0.3, 0.5) were synthesised and characterised. These studies showed that adding more iron (x = 0.3 or 0.5) results in the formation of the tetragonal spinel due to Jahn-Teller distortion of the octahedra, the change in electrical conductivity properties, improved stability of the spinel phase, and that Mn–Cu–Fe oxides can be a promising alternative to the currently used Mn–Co spinels.

Table 1 summarises the available reports on corrosion studies performed on Mn–Cu oxide spinel-based coatings. The studies were performed only for relatively short oxidation times (≤ 2000h). Thus, there is a need to provide long-term data which can validate the practical applicability of the spinel.

Table 1 – Summary of data on Mn–Cu-based coatings available in the literature.

	Coating composition	Substrate material	Temperature of oxidation test	Time of oxidation test	Reference
1	$CuMn_2O_4$	AISI-430 steel	750 °C	100 h	[14]
2	MnCu metallic coatings	SUS 430 steel	800 °C	10 weeks	[15]
3	$Cu_{1.3}Mn_{1.7}O_4$	Crofer 22 APU	800 °C	120 h	[16]
4	$CuMn_{1.8}O_4$	Crofer 22 APU	750 °C, 800 °C	120 h	[17]
5	Mn_2CuO_4	Crofer 22 APU	800 °C	2000 h	[18]
6	$CuFe_2O_4$	SUS 430 steel	800 °C	15 weeks	[19]
7	Copper–Iron coating	Sanergy HT	850 °C	1000 h	[20]
8	$CuFe_2O_4$	Fe–16Cr alloy	800 °C	200 h	[21]
9	$CuFe_2O_4$	Crofer 22 APU	800 °C	600 h	[22]
10	$Cu_{1.3}Mn_{1.7}O_4$	AISI 430	750 °C	500 h	[23]
11	$CuMn_{1.8}O_4$	Crofer 22 APU	800 °C	12 days	[24]
12	$CuMn_2O_4$, $CuNi_{0.2}Mn_{1.8}O_4$	SUS430 steel	700 °C, 800 °C	100 h	[25]
13	$Cu_{1.35}Mn_{1.65}O_4$	460FC steel	700 °C	1000 h	[26]

Please cite this article as: Ignaczak J et al., Fe-modified Mn_2CuO_4 spinel oxides: coatings based on abundant elements for solid oxide cell interconnects, International Journal of Hydrogen Energy, https://doi.org/10.1016/j.ijhydene.2023.06.041

In the present work, three oxides with a general formula of $Mn_{2-x}CuFe_xO_4$, where x = 0, 0.1, 0.3, were electrophoretically deposited on a ferritic stainless-steel support, and their long-term oxidation behaviour was characterised. The protective properties, microstructure and electrical characteristics of the prepared coatings were analysed before and after a high-temperature ageing test. The results were compared to the current state-of-the-art Mn–Co spinel coatings.

Experimental

Powder preparation

Four spinel oxide powders were prepared for this study. The nominal chemical compositions of the powders, the corresponding sample names and stoichiometry calculated from EDX are presented in Table 2.

The powders were synthesised by a modified Pechini method [27,28]. Aqueous nitrate solutions (with known cation concentrations calibrated thermogravimetrically) were mixed in the desired composition ratio. The solutions were heated up to 80 °C, and pre-dissolved aqueous solutions of citric acid and EDTA were added in a molar ratio 2:1:1-TMI (total molar ions). Ammonia solution was gradually added to adjust the pH to ~8. To start the transesterification process, ethylene glycol was added (1 mol of polyalcohol to 1 mol of metal cations). The liquid precursor was then held at 80 °C under continuous stirring until a dense gel was obtained. Further heating up to 200 °C was used to remove any residual water and obtain oxides. The resulting materials were finally calcined at 700 °C for 2 h. More details about the synthesis procedure can be found in Ref. [13]. After calcination, the powders were ground in an agate mortar. For further processing, the particles were then ball-milled in a Fritsch Pulverisette 7 planetary ball mill with 3 mm zirconia balls. The process parameters were set based on the milling machine's manual.

Materials characterisation

Phase composition

The X-ray diffraction (XRD) technique was used to determine the phase composition of the obtained powders and coatings after each stage of processing and after the oxidation tests. The measurements of the coatings were performed on their surfaces. All measurements were conducted at room temperature using a Bruker D2 Phaser 2nd generation diffractometer with CuKα radiation and XE-T detectors. The results were process by the Bruker Topas software.

Table 2 – Chemical composition of powders and sample's name used in this paper.

Nominal composition	Sample name	EDX composition
$MnCo_2O_4$	MCO	$Mn_{0.95}Co_{2.05}O_4$
Mn/Co: 0.5		Mn/Co: 0.46
Mn_2CuO_4	MnCuFe0	$Mn_{2.07}Cu_{0.93}O_4$
Mn/Cu: 2		Mn/Cu: 2.22
$Mn_{1.9}CuFe_{0.1}O_4$	MnCuFe01	$Mn_{1.92}Cu_{0.93}Fe_{0.15}O_4$
Mn/Cu: 1.9		Mn/Cu: 2.06
$Mn_{1.7}CuFe_{0.3}O_4$	MnCuFe03	$Mn_{1.74}Cu_{0.92}Fe_{0.34}O_4$
Mn/Cu: 1.7		Mn/Cu: 1.89

Dilatometric studies

Determinations of the sintering and thermal expansion properties of the materials were carried out using a Netzsch DIL402 dilatometer. Pellets for the thermal expansion measurement with a diameter of 16 mm were prepared by uniaxial pressing of the powders and sintering at 1000 °C. The TEC values were calculated based on the cooling data of the pre-sintered pellets in temperature range 800 °C–100 °C. Measurements were performed in synthetic air with a heating rate of 5 °C/min and a cooling rate of 3 °C/min.

Electrical conductivity of the spinel materials

The electrical conductivities of the pellets were measured with the van der Pauw method. Ceramic pellets were prepared from the ball-milled powders by uniaxial pressing in a hydraulic press (Carver, USA) in a 16 mm (internal diameter) hardened steel die. The powders were compacted using 54 MPa of pressure and sintered at 800 °C in air.

The electrical conductivity measurements were carried out in air in the temperature range of 800 °C down to 200 °C (with decrements/steps of 50 °C). The activation energy of electrical conductivity, E_a, was calculated using the Arrhenius formula:

$$ln\,\sigma T = \frac{-E_a}{k} \times \frac{1}{T} + ln\,\sigma_0 \quad (1)$$

where σ – electrical conductivity, T – temperature, σ_0 – pre-exponential factor, E_a – activation energy, and k – Boltzmann's constant.

The electrical conductivity results are presented including correction for the porosity according to the Bruggeman asymmetric model formula [29]:

$$\sigma = \sigma_m \bullet \frac{1}{(1-p)^{\frac{3}{2}}} \quad (2)$$

where σ – corrected conductivity, σ_m – measured conductivity, and p – sample-pore fraction. The porosity of the pellets was calculated from SEM images using the ImageJ software [30]. Five different SEM images of cross-sections of the pellets were analysed and the porosity was calculated as the average of these images for each sample.

Coating preparation

Deposition of the coatings

The spinel coatings were prepared on stainless steel coupons using the synthesised powders by the Electrophoretic Deposition (EPD) method. Crofer 22 APU alloy (0.3 mm thick, batch number 104754334, VDM-Metals, Germany) was used in this study. Its nominal composition is given in Table 3. The steel coupons were cut into 15 mm × 15 mm x 0.3 mm square specimens. The edges of the samples were rounded with 180-grit SiC paper to remove any post-cutting defects and avoid accelerated oxidation in these areas [31]. The samples were ultrasonically cleaned in deionised water, isopropanol, and acetone to remove surface contaminants (grease and organic compounds).

Using the synthesised powders, four EPD suspensions were prepared. The recipe included 800 ml/L of acetone, 200 ml/L of

Please cite this article as: Ignaczak J et al., Fe-modified Mn_2CuO_4 spinel oxides: coatings based on abundant elements for solid oxide cell interconnects, International Journal of Hydrogen Energy, https://doi.org/10.1016/j.ijhydene.2023.06.041

Table 3 – Chemical composition of used alloy Crofer 22 APU, as provided by VDM-Metals.

	C	S	Cr	Mn	Si	Ti	Cu	Fe	P	Al
Chemical composition (Weight %)	0.002	<0.002	22.81	0.44	0.02	0.08	0.01	76.47	0.003	0.01
EDX composition (Atomic %)	0.13	0.08	21.44	0.61	0.08	0.17	0.78	76.32	0.01	0.38

isopropanol, 10 g/L of the spinel powder, and 0.5 g/L of iodine as a dispersant.

The spinel coatings were deposited in a symmetrical EPD deposition cell in a glass container. The working electrode (specimen) was placed between two counter electrodes with a spacing of 10 mm, which were also made from Crofer 22 APU steel. The deposition parameters were: an applied voltage of 60 V, and a deposition time of 60 s. After the deposition, the samples were dried in air for 2 h. In total, 20 specimens of each type were prepared. For quality control, the weight of the dry deposits was measured.

Sintering of the coatings

The coatings were sintered via a two-stage procedure, which is typical for spinel interconnect coatings [32,33]. Prior to starting the process, an investigation of the effect of temperature was carried out (Fig. S1), and the final sintering conditions were chosen based on these results. First, the coated samples were heated in a tube furnace in a dry hydrogen atmosphere at 1000 °C for 10 h to reduce the spinel oxide. In the second stage, the samples were reoxidation at 800 °C for 2 h in static air in a muffle furnace.

Oxidation experiments

In this study, two different types of reference samples were used: non-coated steel coupons and pre-oxidised steel coupons. The non-coated coupons were used in their "raw" form, while the pre-oxidised samples were chemically treated prior to the high-temperature ageing tests. The treatment mimicked the two-stage sintering procedure described in section Sintering of the coatings but performed on an uncoated steel coupon.

The cyclic oxidation experiment was carried out at 750 °C in static air, 15 samples of each kind were used for this evaluation. At the beginning, when higher mass gain was expected, shorter oxidation cycles were applied: 50 h, 100 h, 100 h. Afterwards, each cycle lasted 250 h until the samples reached 3000 h at 750 °C. After each cycle, the weight gain was determined using a Radwag analytical balance with a 0.1 μg resolution.

Table 4 – Parabolic oxidation rate constant of all the investigated samples oxidised for 3000 h in air at 750 °C (For the reference samples, two values of k_p were calculated, for two time ranges: 0–500 h and 500–3000 h).

	k_p [$g^2\ cm^{-4}\ s^{-1}$]	$k_p$sample/$k_p$ref
Reference	3.76E-15/2.28E-14	1
Reference – preox	3.25E-15	0.14
MnCuFe0	6.1E-15	0.27
MnCuFe01	4.92E-15	0.22
MnCuFe03	4.73E-15	0.21
MCO	5.22E-16	0.02

Sample analyses

Area specific resistance measurements

The electrical performance of the coated and uncoated samples was evaluated by ASR testing as a function of temperature (750 °C – 300 °C) in air (one measurement on each kind of sample). For the ASR measurement, circular platinum contacts with a diameter of 5 mm were applied in the centre of the spinel-coated samples from both sides. The platinum paste was dried at 100 °C on a hot plate and then the samples were heated up to 750 °C for 10 min. The measurement was carried out in a four-wire two-electrode system using a 1 Hz sinusoidal signal (Gamry 1010 analyser). The samples were heated up to 750 °C, and then cooled to 200 °C with simultaneous impedance measurement performed every 50 °C. These measurements determined the ASR (surface resistance) of the samples after different oxidation periods. The results were calculated for the area of the platinum contact according to the formula:

$$ASR = \frac{R \cdot A}{2} \quad (3)$$

Where: R – electrical resistance [Ω], and A – surface area of the Pt layer [cm^2].

Coating characterisation

SEM

The sample surface and cross-section microstructure before and after the oxidation tests (for periods of 250 h, 1000 h and 3000 h) were characterised by a Thermo Fisher Phenom XL scanning electron microscope (SEM) equipped with an energy dispersive X-ray (EDX) detector. The cross-sections for the SEM and EDX analyses were prepared using epoxy embedding and were polished to a 1 μm diamond finish and carbon-coated.

TEM

An FEI Tecnai G^2 T20 transmission electron microscope (TEM), operated at 200 kV, was used for electron diffraction, TEM bright field (BF) and dark field (DF) imaging, scanning TEM (STEM) imaging, as well as EDX analysis. The TEM specimens were prepared using an FEI Versa3D focused ion beam – scanning electron microscope (FIB-SEM). For the final polishing of the TEM specimens, a low voltage (2 kV) ion beam was used to minimise damage from sample preparation.

Synchrotron multimodal chemical imaging with micro-focused X-ray beam

X-ray diffraction- and X-ray fluorescence – contrast microscopy was performed at the microXAS beamline of the Swiss Light Source (SLS) at the Paul Scherrer Institute. Images were acquired by raster scanning of the samples with an X-ray beam with an energy of 18.2 keV focused to a 1 × 1 μm^2 spot

Please cite this article as: Ignaczak J et al., Fe-modified Mn_2CuO_4 spinel oxides: coatings based on abundant elements for solid oxide cell interconnects, International Journal of Hydrogen Energy, https://doi.org/10.1016/j.ijhydene.2023.06.041

size. The XRF spectra and XRD patterns were measured simultaneously in transmission mode with a dwell-time of 200 ms per point. For each image pixel, data were acquired using two SDD detectors for XRF and an Eiger4M (Dectris) 2D detector for XRD. The diffraction measurements were calibrated by measurement of the LaB_6 standard. The XRD data in the format of images of diffraction rings was first azimuthally integrated using the PyFAI python library [34], followed by an analysis performed using the XRDUA software [http://xrdua.ua.ac.be/]. The XRF spectra were analysed using the PyMca software [35]. Samples for the XRD – and XRF – contrast microscopy were prepared by Plasma-FIB milling in the form of lamellas with a thickness of about 50 μm (Fig. S2).

Results and discussion

Powder characterisation

Chemical and morphological analysis of the powders

In this work, four powders were synthesised by the sol-gel technique based on combined CA and EDTA chelating agents. It is an effective technique for multi-cation oxides, ensuring uniform cation distribution [36].

Fig. 1a presents an ex-situ XRD phase analysis of the MnCuFe0, MnCuFe01, MnCuFe03, and MCO as-synthesised powders (2 h of calcination in air at 700 °C, before the milling step). The samples containing copper reveal a two-phase composition: cubic spinel phase (space group Fd-3m) and Mn_2O_3 (bixbyite, space group Ia-3). The cobalt–manganese spinel consists of a single phase (cubic phase Fd-3m). These results are consistent with the data reported by F. Afrani et al. [37]. Mn_2CuO_4 synthesised at 700 °C consists of a spinel with secondary phases of α-Mn_2O_3 and Cu, whereas the higher calcination temperature produced a single phase spinel.

A high-energy milling process carried out in a planetary mill led to a reduction of the crystallite size, which was evaluated based on a peak broadening analysis. XRD patterns suggest a significant comminution of the powders. The XRD patterns obtained after this step are presented in the supplementary materials in Fig. S3. For the milled powder, the phase composition remained the same as the as-synthesised powder.

Dilatometry study

Fig. 1c illustrates the sintering behaviour of the materials. The shrinkage of the MnCuFex materials starts at 755 °C–818 °C, depending on the iron content. Cu–Mn based materials show a lower sintering onset temperature than Co–Mn spinel. At

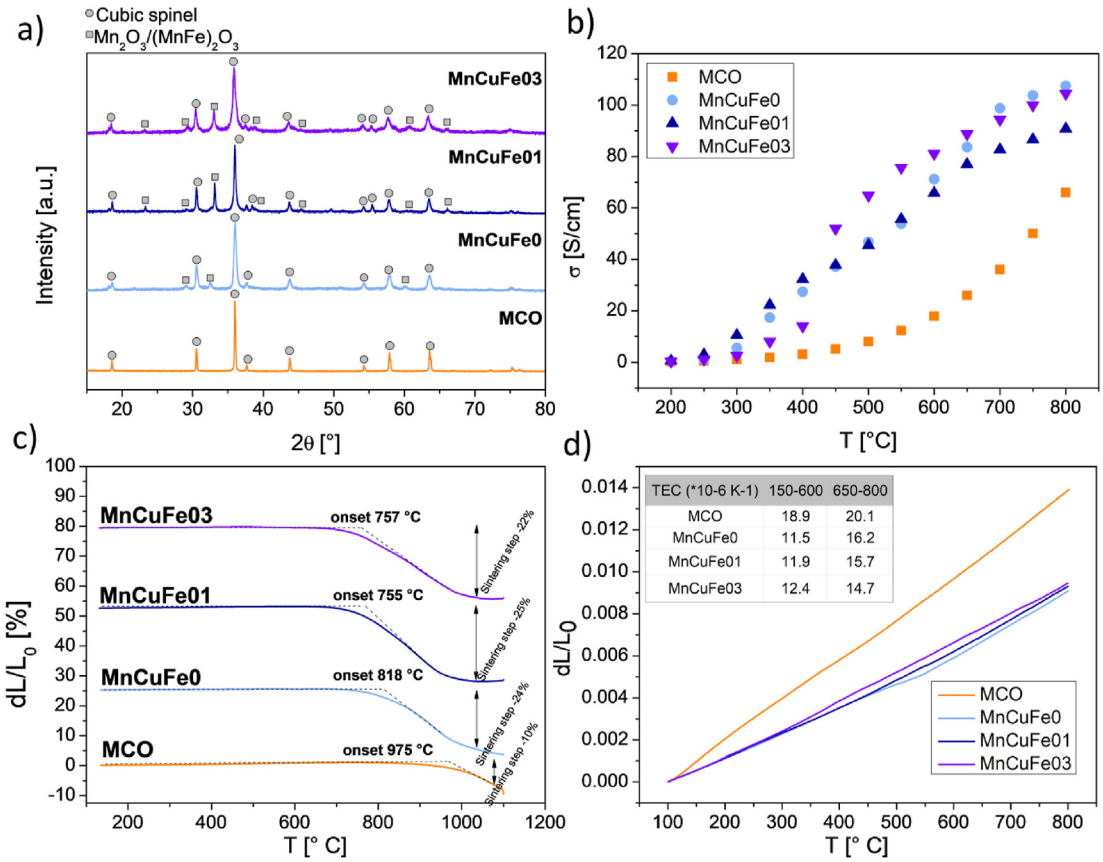

Fig. 1 – Powder characterisation: a) XRD patterns of synthesised powders after calcination at 700 °C obtained with CuKα; b) electrical conductivity of pellets as a function of the temperature; the results were corrected for sample porosity; c) dilatometry of the oxide pellets, pre-sintered at 1000 °C; d) TEC values calculated for the two temperature ranges are shown in the inset table.

Please cite this article as: Ignaczak J et al., Fe-modified Mn_2CuO_4 spinel oxides: coatings based on abundant elements for solid oxide cell interconnects, International Journal of Hydrogen Energy, https://doi.org/10.1016/j.ijhydene.2023.06.041

1100 °C (maximum sintering temperature), the sintering of the MnCuFex pellets seems to be accomplished, since there is no further change in the dimensions of the pellets and the obtained shrinkage is in the range 22–25%, while for the MCO pellets, the process did not finish.

In comparison to MCO, MnCuFex materials show a substantial reduction in the onset temperature and increased shrinkage at elevated temperatures. Cu–Mn spinels show enhanced sintering properties. Partly replacing Mn by Fe affects the sintering behaviour by further lowering the onset temperature and reaching the final shrinkage at a lower temperature.

Thermal expansion measurements are shown in Fig. 1d. The calculated TEC values are summarised in the inset table in the same figure. The TEC values were calculated by linear fitting in two temperature ranges, a lower one from 150 °C to 600 °C and a higher one from 650 °C to 800 °C.

For the MnCuFe0 sample, the transition point on thermal expansion is the most visible and the values of TEC calculated for lower temperatures and for higher temperatures differ the most, at 11.5 10^{-6} K^{-1} and 16.2 10^{-6} K^{-1}, respectively. For material containing the highest fraction of Fe (MnCuFe03) the transition point on thermal expansion is least visible and differences between values calculated for two temperature ranges also differs the least. The TEC calculated for all MnCuFex pellets is lower than these calculated for the MCO pellet. Value of TEC obtained for state of the art material is higher than reported before [38,39], this can be due to poor sintering, bigger particle size obtained after milling step than for MnCuFe oxides. Lowering the TEC at high temperatures makes this material more suitable for applications as a protective coating for interconnectors, used in this study alloy Crofer 22 APU exhibits the TEC of 11.5 10^{-6} K^{-1} [40]For SOFCs operating at high temperatures, which are exposed to thermal cycling, good matching of the interconnect TEC and coating TEC is essential for the mechanical stability of the coating, and thus for its performance.

Electrical conductivity characterisation

The electrical conductivity of the synthetised materials was measured in the temperature range 200–800 °C in air. The results are presented in Fig. 1b. MnCuFex materials show quite similar electrical behaviour with a monotonic increase of conductivity on heating and a maximum conductivity of 90–110 S cm^{-1} at 800 °C. There is no relation between the conductivity and iron content in MnCuFex oxides, which indicates that the higher ratio Cu/Mn favours the concentration of Mn^{3+}/Mn^{4+} ions that participate in the electronic conductivity through small polaron hoping between the octahedral sites [41]. The maximum conductivity for MCO spinel is 60 S cm^{-1} at 800 °C. At an intermediate temperature range (500–600 °C), the electrical conductivity of the MnCuFex spinels is 2–3 times higher than the conductivity of the MCO spinel. At high temperatures, the differences in conductivity are minor. These materials are therefore promising for applications as intermediate temperature protective coatings.

In our previous work, where the copper was substituted with Fe ($Mn_{1.7}Cu_{1.3-x}Fe_xO_4$), the electrical conductivity of the pellets was higher (~180 S cm^{-1} at 650 °C for $Mn_{1.7}Cu_{1.3}O_4$ and $Mn_{1.7}Cu_{1.2}Fe_{0.1}O_4$ samples), but the materials were not phase stable and CuO precipitated at temperatures higher than 650 °C, causing lowering of the conductivity above this temperature [13]. Substitution of Fe in place of Mn, as studied in this work, increases the stability of the material at the expense of the electrical conductivity.

The Arrhenius plots for electrical conductivity are shown in Fig. S4. The activation energies were calculated for two temperature ranges 200 °C–400 °C and 450 °C–800 °C, similar as for the dilatometric measurement. Results are summarised in table insert in the same figure. The observed trend for MnCuFe samples is in agreement with previous findings, reported in our previous work [13]. At high temperatures, the activation energies were low compared to the values calculated for low temperature regime. There is a clear dependence between the iron content and activation energies, which decrease with increasing amount of iron. For the MCO spinel, for the temperature range 200 °C–400 °C the value is 0.356 eV and 450 °C–800 °C is 0.49 eV.

Coated samples preparation

To achieve a satisfactory density, spinel coatings are typically sintered in a two-step process. The first step is the reduction of the coating, where the oxide is reduced, followed by the second step, the reoxidation, where the spinel should re-form. In the case of MnCo spinel, the sintering conditions have been studied extensively [33,42,43], whereas for MnCu spinels, such studies are not yet reported. The summary of the sintering deposition processes and the sintering conditions used for the preparation of the spinel coatings is given in Table S1.

In the case of the MnCuFe03 coatings, the microstructure of the coating after the reduction (10 h in H_2 at 1000 °C) and reoxidation (2 h in air at 800 °C) steps are presented in Fig. 2a and b, respectively. The reduced sample shows a porous structure and the presence of metallic particles (Fe + Cu) and MnO, as also confirmed by XRD (Fig. 2d). Exposure to high temperatures also results in the formation of interfacial oxide scale. In the case of the MnCuFe0 and MnCuFe01, the microstructures are similar (not shown here). In the case of the MCO spinel, the reduction leads to the formation of metallic Co and MnO. The reoxidation step leads to densification of the coatings, as is visible in Fig. 2b. The final density of the coatings depends strongly on the initial reduction conditions, as presented in Fig. S1. A clear relationship can be seen between the metallic grain size and low porosity. Similar results were obtained by Bobruk et al. [33] in their MCO spinel sintering study. Based on these results, the reduction temperature of 1000 °C was selected, as it results in a high final density of the coatings.

To check the phase composition after the densification process, XRD analysis was performed for the final samples, which is presented in Fig. 2e. The analysis showed that the MnCuFe01 and MnCuFe03 samples are single phase and are crystallised in the cubic spinel phase with a Fd-3m space group. The diffraction peaks corresponding to this phase are slightly shifted to higher diffraction angles as compared to that of the $MnCo_2O_4$ coating due to the replacement of Co with Mn, Cu and Fe [39]. The MnCuFe0 coating also features a second phase – Mn_2O_3.

To evaluate how the sintering conditions affect the mass change, the samples' masses were measured after each stage

Please cite this article as: Ignaczak J et al., Fe-modified Mn_2CuO_4 spinel oxides: coatings based on abundant elements for solid oxide cell interconnects, International Journal of Hydrogen Energy, https://doi.org/10.1016/j.ijhydene.2023.06.041

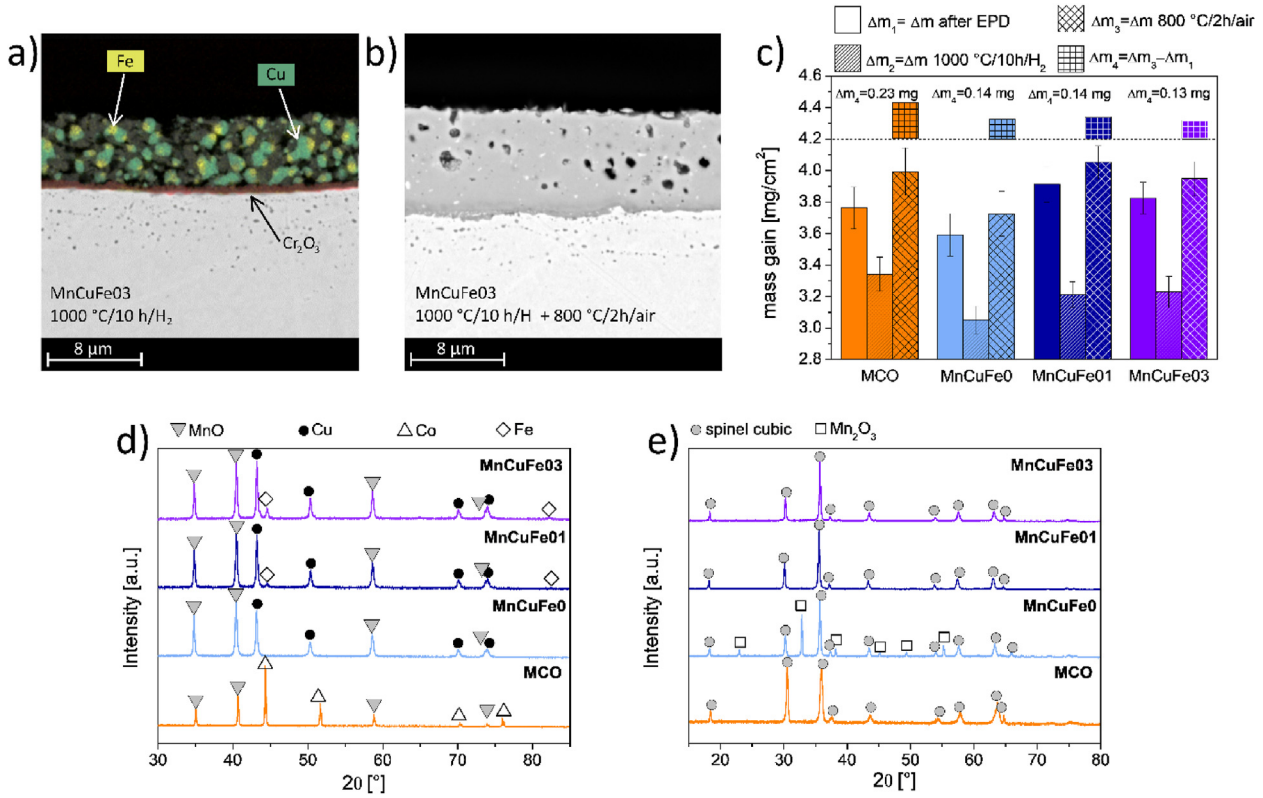

Fig. 2 – a) SEM images of reduced MnCuFe03 coating, b) SEM images of the MnCuFe03 coating after sintering treatment, c) Mass gain measured during the coating preparation, d) XRD pattern of the coatings after the reduction step, e) XRD pattern of the coatings after the sintering treatment.

of sample preparation. The results are presented in Fig. 2c. The first bar for each sample type corresponds to the mass of powder deposited by means of electrophoretic deposition on 1 cm^2. The obtained values are at the same level and should produce coatings of approximately the same thickness, which simplifies determining the corrosion properties of the different materials.

The second bar of mass change corresponds to the mass of the samples after the first step of the sintering process, namely sintering in dry hydrogen at 1000 °C for 10 h. There is a noticeable decrease in the mass of each sample, which is due to the above-described phenomena of reduction of the coating. At the same time, it should be noted that under these conditions, the steel is oxidised and high-temperature corrosion products are formed on its surface, as is illustrated by the SEM image of the MnCuFe03 layer (Fig. 2b).

The third bar represents the weight gain after the second sintering step, when the spinel structure reforms, and further oxidation of the substrate material occurs. The difference between Δm_3 and Δm_1 represent the mass of the corrosion product and is shown in the graph above other bars. The thickness of chromium oxides was calculated from these values, assuming that only chromium oxide is formed, since the ratio of the formed spinel $MnCr_2O_4$ to Cr_2O_3 is unknown. Accepting this simplification introduces an error of 25% at most. These data are shown in Table 5. The thickness of the oxide scale formed during the sintering process on steel coated with a MnCuFe0 spinel coating is 0.80 µm, for MnCuFe01 – 0.85 µm, for MnCuFe03 – 0.75 µm, and for MCO – 0.97 µm. These values are comparable with coatings containing copper and smaller than for uncoated steel sintered under the same conditions, for which the thickness of corrosion products is 1.16 µm.

Microstructures of the as-prepared samples

Fig. 3a depicts SEM images of cross-sections of the MCO and $Mn_{2-x}CuFe_xO_4$ spinel coatings deposited by EPD after the two-step heat treatment under selected conditions. The obtained coatings have a similar thickness of about 12 µm. Only the MCO has a slightly lower thickness of about 8 µm. The porosity of the coatings is low and ranges from 6% to 15%, depending

Table 5 – Thickness of oxide scale after peroxidation treatment and after 3000 h oxidation test at 750 °C.

		ref-preoxidated	reference	MnCuFe0	MnCuFe01	MnCuFe03	MCO
thickness of the oxide scale [µm]	Sintering treatment	1.16	–	0.80	0.85	0.75	1.40
	After oxidation (3000 h)	1.14	2.85	1.63	1.41	1.38	0.41
	Total thickness	2.30	2.85	2.43	2.26	2.18	1.81

Please cite this article as: Ignaczak J et al., Fe-modified Mn_2CuO_4 spinel oxides: coatings based on abundant elements for solid oxide cell interconnects, International Journal of Hydrogen Energy, https://doi.org/10.1016/j.ijhydene.2023.06.041

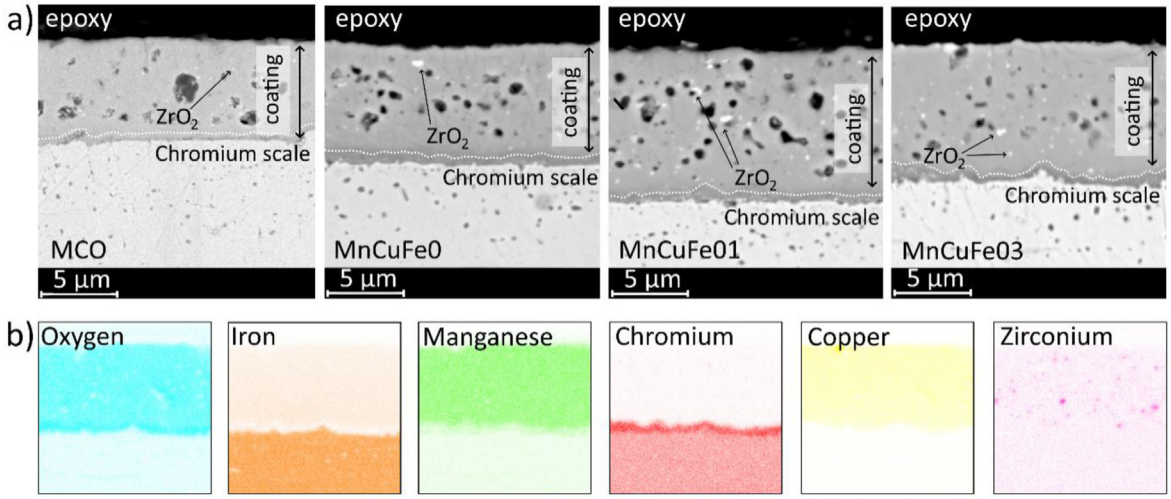

Fig. 3 – a) SEM images of the cross-sections of each type of the coatings obtained after sintering treatment; b) EDX map analysis of the MnCuFe03 coating.

on the iron content, which significantly influences the porosity. The lowest porosity of 6% was achieved for the MnCuFe03 coating.

EDX analysis for the MnCuFe03 coating shown in Fig. 3b revealed that the formed oxide scale was mainly composed of Cr and O with a minor addition of Mn. It has been reported in previous research that oxidation of ferritic stainless steel leads to the formation of a dual scale of corrosion product: Cr_2O_3 and a top layer of $(MnCr)_3O_4$ spinel [44,45].

No chromium content was detected in the inner part of the coating, and no reaction layer between the oxide scale and the spinel was observed.

The particles of ZrO_2 visible in Fig. 3 are contamination from the high-energy ball milling process. The ZrO_2 particles can be used as an indicator of the direction of the diffusion process that occurs during oxidation.

The manganese-cobalt spinel coatings prepared as the reference coating also show low porosity and a morphology similar to $Mn_{2-x}CuFe_xO_4$. According to the SEM analysis, the thickness of the oxide scale is also 1–2 µm.

EDX scans were also performed on the surface of the as-prepared samples (Table 6). The atomic composition of the MnCuFex coating after sintering differs from that of the raw powder; the ratio of manganese to copper in each of these

Table 6 – Element atomic concentration, collected from the surfaces of the coated samples after 0 h, 250 h, 1000 h, 3000 h of oxidation at 750 °C.

0 h	O [at. %]	Mn [at. %]	Cu/Co [at. %]	Fe [at. %]	Cr [at. %]	Mn/Cu calculated from EDX	Mn/Cu from powder stoichiometry
MCO	71.6	9.5	18.5	0.3	0.1		
MnCuFe0	70.9	17.3	11.0	0.5	0.2	1.6	2
MnCuFe01	69.2	17.6	11.7	1.3	0.1	1.5	1.9
MnCuFe03	69.1	15.4	11.5	3.6	0.2	1.3	1.7
250 h							
	O	Mn	Cu/Co	Fe	Cr	Mn/Cu	Mn/Cu
MCO	70.8	9.4	18.3	1.6	0.3		
MnCuFe0	71.2	19.6	10.4	0.9	0.2	1.9	2
MnCuFe01	69.5	18.3	11.2	1.5	0.2	1.6	1.9
MnCuFe03	69.4	17.1	10.2	4.0	0.2	1.7	1.7
1000 h							
	O	Mn	Cu/Co	Fe	Cr	Mn/Cu	Mn/Cu
MCO	70.8	9.6	16.8	2.3	0.5		
MnCuFe0	70.1	19.5	8.7	1.3	0.3	2.3	2
MnCuFe01	70.6	17.2	9.5	1.9	0.3	1.8	1.9
MnCuFe03	68.9	16.5	10.0	4.2	0.3	1.7	1.7
3000 h							
	O	Mn	Cu/Co	Fe	Cr	Mn/Cu	Mn/Cu
MCO	70.6	9.5	16.4	2.6	0.9		
MnCuFe0	71.7	20.3	5.8	1.8	0.4	3.5	2
MnCuFe01	68.9	21.6	6.3	3.0	0.3	3.4	1.9
MnCuFe03	69.6	16.6	9.5	4.0	0.4	1.7	1.7

Please cite this article as: Ignaczak J et al., Fe-modified Mn_2CuO_4 spinel oxides: coatings based on abundant elements for solid oxide cell interconnects, International Journal of Hydrogen Energy, https://doi.org/10.1016/j.ijhydene.2023.06.041

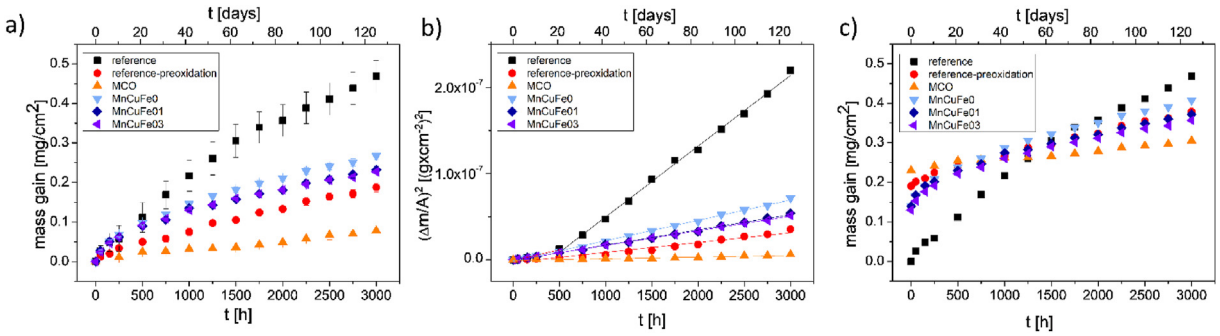

Fig. 4 – Weight gain of the samples plotted on linear a) and parabolic b) scales; c) mass gain shifted by mass increase caused by coatings' sintering process.

coatings is lower than in the raw powder stoichiometry, indicating a larger concentration of copper on the top of the coating. This observation may be related to the low melting point of metallic copper and the subsequent high vapour pressure. It is worth pointing out that metallic copper particles are present after the first sintering phase, and copper vaporisation to the upper section of the coating is feasible during this stage. Further evidence that there is a larger concentration of copper near the surface rather than a loss of manganese from the sample comes from the fact that a similar effect is not visible for the MCO coating. Each coating contains only trace amounts of Cr.

Oxidation kinetics

The mass change of all coated samples caused by the long-term oxidation is shown in Fig. 4 in linear (a) and parabolic (b) plots (mass change caused by the sintering process is not included in this plot). According to the data collected in Table 1, 3000 h is the longest evaluated time of oxidation for coatings based on Mn–Cu oxide until now.

With a good linear approximation in Fig. 4b, the mass change can be described by the parabolic kinetics, indicating that oxide scale growth is controlled by the solid-state diffusion.

The uncoated steel samples (reference with no pre-sintering treatment) showed the highest parabolic rate constant, and the samples coated with the MCO coating showed the lowest one (Table 4). It is worth pointing out that for this type of samples, the parabolic oxidation rate constant is calculated for time ranges from 0 h up to 500 h and from 500 h to 3000 h, since there is an evident change in the slope of the line in Fig. 4b, and this phenomenon was already observed for uncoated FSS [46]. The values of mass weight gain for samples coated with $Mn_{2-x}CuFe_xO_4$ are intermediate, and among these samples, the highest weight gain was observed for the samples coated with the MnCuFe0 spinel.

In addition to the reference, uncoated and untreated steel samples, pre-oxidised steel samples (without coatings) were also used in the oxidation experiment, which were marked as reference-preoxidised. This was performed to evaluate the potential influence of the initial heat treatment (coating sintering steps) of the alloys on their apparent weight gain during the long-term oxidation. Thus, the reference-preoxidised samples were subjected to the same heat treatment as the coated samples.

According to Fig. 4a, the reference-preoxidised samples showed the lowest weight gain among the tested samples; lower even than the coated ones. This result is, however, deceptive, as these values do not include the initially formed oxide scale, which increased the weight gain. Similar effects also influence the weight gain data of the other samples.

The corrected weight gains of the coated and reference samples, including their initial weight gain, are presented in Fig. 4c. Also, the mass gain of the reference-preoxidised sample during heat treatment is shown in Fig. S5. After 1000 h, all the curves seem to converge and the differences between them become smaller. The lowest total weight gain was achieved for the MCO-coated samples. The weight gain of the MnCuFex samples was similar to the weight gain of the uncoated alloys. According to the literature and previous experiments, it must be taken into account the mass gain error for uncoated samples associated with chromium evaporation. H. Falk-Windish et al. [47] have reported chromium evaporation data for ferritic stainless steel Crofer 22H at 750 °C and after 500 h of oxidation obtain value of ~0.07 mg/cm^2. There is not experimental data for particular one alloy and condition of oxidation used in this study. Chromium evaporation for Crofer 22 APU was examined at 850 °C and at 800 °C, after 500 h achieved 0.078 mg/cm^2 and 0.054 mg/cm^2 respectively [48,49].Taking into account possible Cr-evaporation from the reference and the reference-preoxidised sample, the weight gain for the latter would be approaching the MnCuFe0 sample weight gain. Thus, the preoxidised-reference and MnCuFex showed virtually the same weight gain. This leads us to an important conclusion, that the MnCuFe0 spinel do not reduce the corrosion rate (oxide scale growth), which to some degree is observed for the MnCuFe03 and which apparently is the case for the MCO spinel.

Based on the weight gain data, the oxide scale thickness, including the initial thickness and the long-term oxidation-formed thickness, could be calculated. These results are summarised in Table 5. After the 3000-h-long oxidation at 750 °C, the total oxide thickness of the MnCuFex samples is similar to the reference-preoxidised. The reference sample shows the highest oxide scale thickness, possibly due to the effect of the oxide scale microstructure. Chromia oxide formed at a higher temperature (in the case of the preoxidised-reference) will have larger crystallites and fewer grain boundaries, resulting in a lower weight gain/oxide thickness. These effects were studied, e.g., by Talic et al. [50].

Please cite this article as: Ignaczak J et al., Fe-modified Mn_2CuO_4 spinel oxides: coatings based on abundant elements for solid oxide cell interconnects, International Journal of Hydrogen Energy, https://doi.org/10.1016/j.ijhydene.2023.06.041

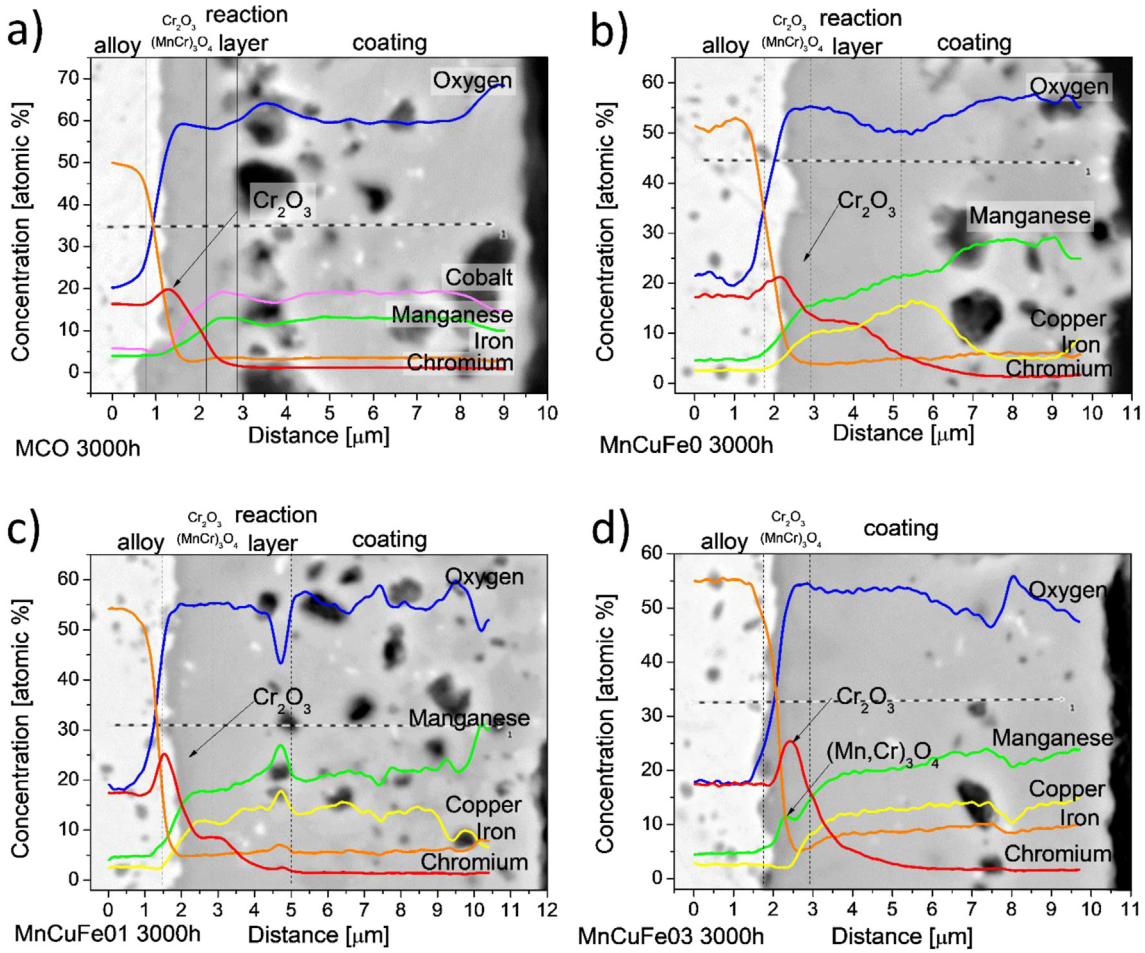

Fig. 5 – SEM images of coating after 3000 h of oxidation at 750 °C including results of EDX line scans through the entire coating thickness for a) MCO, b) MnCuFe0, c) MnCuFe01, and d) MnCuFe03.

Based on the weight gain results and the calculated oxide scale thickness, it can be assumed that the MnCuFex materials do not slow down the corrosion process to the same extent as the currently used $MnCo_2O_4$. There is a clear difference in the oxidation kinetics between the samples coated with materials containing manganese-copper-iron and manganese-cobalt. The parabolic oxidation rate constants were calculated from the plot presented in Fig. 4b and are collected in Table 4. The K_p and the ratio of the k_p of a specific sample to the reference samples is the lowest for the MCO coating and is 10 times lower than for the MnCuFex coating. Based on these results, it can be concluded that the corrosion rate for samples with Mn–Cu–Fe is reduced by a factor of 5, and for samples with Mn–Co by a factor of 50.

The chromia scale thickness calculated from the weight gains can be compared with the thickness from the SEM imaging, presented on Fig. 5. The calculated values assume that mass gain is caused only by formation of pure Cr_2O_3. According to EDX line scan, the chromia thickness for the MCO coated samples is 1.5 μm and is in good agreement with weight gain data.

For MnCuFe0 and MnCuFe01 samples, the Cr-profiles are more complicated due to more complex reaction layer. In the first layer, the Cr_2O_3 with thickness of ~1.5 μm can be observed, where chromium content is up to ~25%. Beyond, the Cr content drops to a level of 15% and 8% for MnCuFe0 and MnCuFe01 respectively and remains at that level for the next ~6 μm.

The MnCuFe03 sample exhibits different distribution of chromium: maximum concentration is in line with presence of Cr_2O_3, increases to ~25% and then declines exponentially, which points that addition of iron can effectively slow down diffusion of chromium to the external Mn–Cu oxide layer.

Postmortem characterisation after oxidation for 3000 h at 750 °C

Electron microscopy characterisation

Fig. 5 shows SEM images combined with the line scan EDX analysis of a cross-section after 3000 h of oxidation. All the samples exhibited good adhesion of the coating to the steel. A dense reaction layer structure has been observed next to the chromia scale for MnCuFe0 and MnCuFe01. For samples coated with MnCuFe0 and MnCuFe01, lighter and darker regions could be observed in the BSE-SEM images in the outer part of the coating. The MnCuFe03-coated sample seems to have a uniform structure with no reaction layer.

Please cite this article as: Ignaczak J et al., Fe-modified Mn_2CuO_4 spinel oxides: coatings based on abundant elements for solid oxide cell interconnects, International Journal of Hydrogen Energy, https://doi.org/10.1016/j.ijhydene.2023.06.041

Linear EDX scan confirms the increase in thickness of the corrosion product-chromia scale compared to the as-prepared samples. They reached a thickness of about 2 μm for the MnCuFe0 layer, and about 1.5 μm for the MnCuFe03 layer. An important finding is the absence of a thick reaction layer between the coating and chromium scale for the MnCuFe03 coating. In contrast, for the MnCuFe0 samples, a 2-μm-thick reaction layer with a high chromium content of about 15% atomic is observed.

The structure of the MnCuFe03 does not change significantly on oxidation, as it maintains low porosity and no cation segregation is observed. The EDX point analysis performed in three locations of the cross-section shows that the coating has retained its original stoichiometry and confirms that the chromium concentration in the inner part of the layer is higher than the outer, which is consistent with the line scan.

The surface chemical composition was also analysed by EDX (at a low magnification of 1000 from 3 different locations on the samples) for samples after 0 h, 250 h, 1000 h, 3000 h of oxidation, which is summarised in Table 6.

EDX Surface analysis of the EPD-coated samples indicates presence of chromium right at the beginning of the oxidation experiment (0.2–0.5 wt%, within the limit of detection). For the MCO sample, an increase of the chromium amount is observed over time, to reach a maximum of 0.5% after 3000 h of exposure. All the measured values of Cr content are very low, and it can be concluded that the surface chromium concentration in each of the obtained coatings is negligible.

Data about the ratio of manganese to copper in the MnCuFe0, MnCuFe01, MnCuFe03 was also obtained from the surface EDX study. After sintering, the ratio of Mn to Cu is lower than that resulting from the stoichiometry of the deposited powder, which was discussed earlier in the subsection-as prepared coating. With oxidation time, the manganese content increased while the copper content decreased significantly for the MnCuFe0 and MnCuFe01 samples. For the MnCuFe03 sample, these values remained constant and correspond to the stoichiometry of the powder from which the coatings were prepared. Thus, the MnCuFe03 coatings appear to be significantly more chemically stable than the other MnCuFex coatings.

XRD study presented in Fig. S6 showed the presence of Mn_2O_3 in the MnCuFe0 and MnCuFe01 coatings. In the case of the MnCuFe0 coating, manganese oxide was present immediately after the sintering step and after 3000 h of testing, the amount of this phase has further increased. Before the oxidation process, the MnCuFe01 coating consisted only of one spinel cubic phase, but during the oxidation, a second, Mn_2O_3 phase appeared, and similarly to the MnCuFe0, its amount increased during further processing. The XRD study of the MnCuFe03 showed the sole presence of the spinel cubic phase before the start of the oxidation process. After 3000 h of oxidation, the presence of another phase could be detected, however due to the low signal-to-noise ratio, it was impossible to identify this phase using traditional XRD measurements performed on the surface of the samples.

Transmission electron microscope observation

To examine the coating microstructure in detail and the differences between the coating without iron and with iron content, a TEM analysis, including (S)TEM imaging and STEM-EDX mapping, was carried out for the MnCuFe0 and MnCuFe03 samples after 3000 h of oxidation at 750 °C.

Fig. 6a shows a STEM image and EDX elemental maps at the interface between the substrate and the coating layer in the MnCuFe0 sample. A corrosion product layer, which predominantly consists of Cr and O, can be observed at the interface. This corrosion layer has a thickness of ~0.5 μm. Above this layer, the chromium elemental distribution in the EDX map also indicates that there is a thicker interlayer of ~1 μm with a

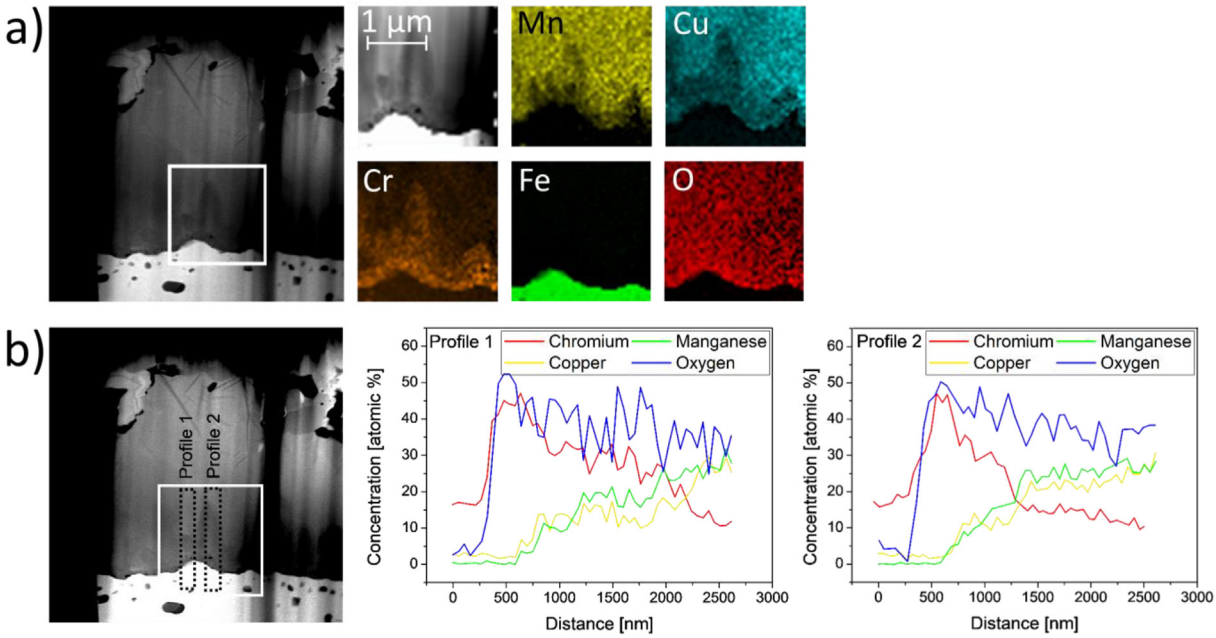

Fig. 6 – a) STEM image of the MnCuFe0-coated coupon and the element distribution map generated for the marked area, b) EDX line scans performed from the interface between the substrate and coating.

Please cite this article as: Ignaczak J et al., Fe-modified Mn_2CuO_4 spinel oxides: coatings based on abundant elements for solid oxide cell interconnects, International Journal of Hydrogen Energy, https://doi.org/10.1016/j.ijhydene.2023.06.041

chromium concentration (30 at. %) slightly lower than that in the corrosion product layer, according to line scans shown in Fig. 6b. In addition, Mn and Cu exist in this region, both with concentrations of ~20 at. %. Further above this layer in the coating film, the chromium content is significantly deceased, which is consistent with the SEM measurements shown in Fig. 5b. It is worth noting that the distribution of Mn and Cu differs slightly, which may prove the presence of $(Mn,Cr)_3O_4$ as a second component of the corrosion product.

Fig. 7a shows a TEM lamella obtained by FIB for high-resolution element distribution analysis, and three element maps made with different magnifications and from different areas on the MnCuFe03 sample. The squares on the STEM image of the lamella illustrate the areas from which the distribution maps of the selected elements (Cr, Mn, Cu, Fe, O) were obtained. The map made on the surface between the coating and substrate confirms the presence of Cr_2O_3 as the main component of the corrosion product. Above this oxide, a thinner layer of $(Mn, Cr)O_4$ can be seen, the forming of which is characteristic for the Crofer 22 APU alloy [45]. The element distribution from the top part of the coating presented in the middle row shows an even distribution of elements with a marked border for the chromium reaction layer, above which the presence of chromium is not detected. It is worth noting that the contrast in the Cr map in the first row is due to noise in the EDX measurements. Based on these observations, it can be concluded that chromium species are efficiently stopped from evaporation by reaction with the coating, forming $(Mn, Cu, Cr)_3O_4$ spinel oxide.

EDX mapping at a higher magnification reveals the uneven distribution of iron and copper at the nanometre scale. The cation distribution maps reveal unexpected cation segregation, which gives rise to needle-like structures in the coating, as shown in Fig. 7b. EDX maps show a homogeneous distribution of oxygen and manganese, but different copper and iron contents. In places, where the copper content is lower, there is more iron, and vice versa (Fig. 7d). This so-called needle structure is present throughout the whole volume of the coating.

Fig. 7c presents a selected area electron diffraction pattern made on a single crystal grain that contains the needle-like structure (on the area marked on images above the diffraction pattern). This pattern corresponds to the spinel structure and shows a single structure phase in the coating in spite of the Cu and Fe segregation. However, the presence of a second phase cannot be ruled out and the resulting electron diffraction pattern could not reveal of presence of the second phase. According to XRD patterns made from the surface of this

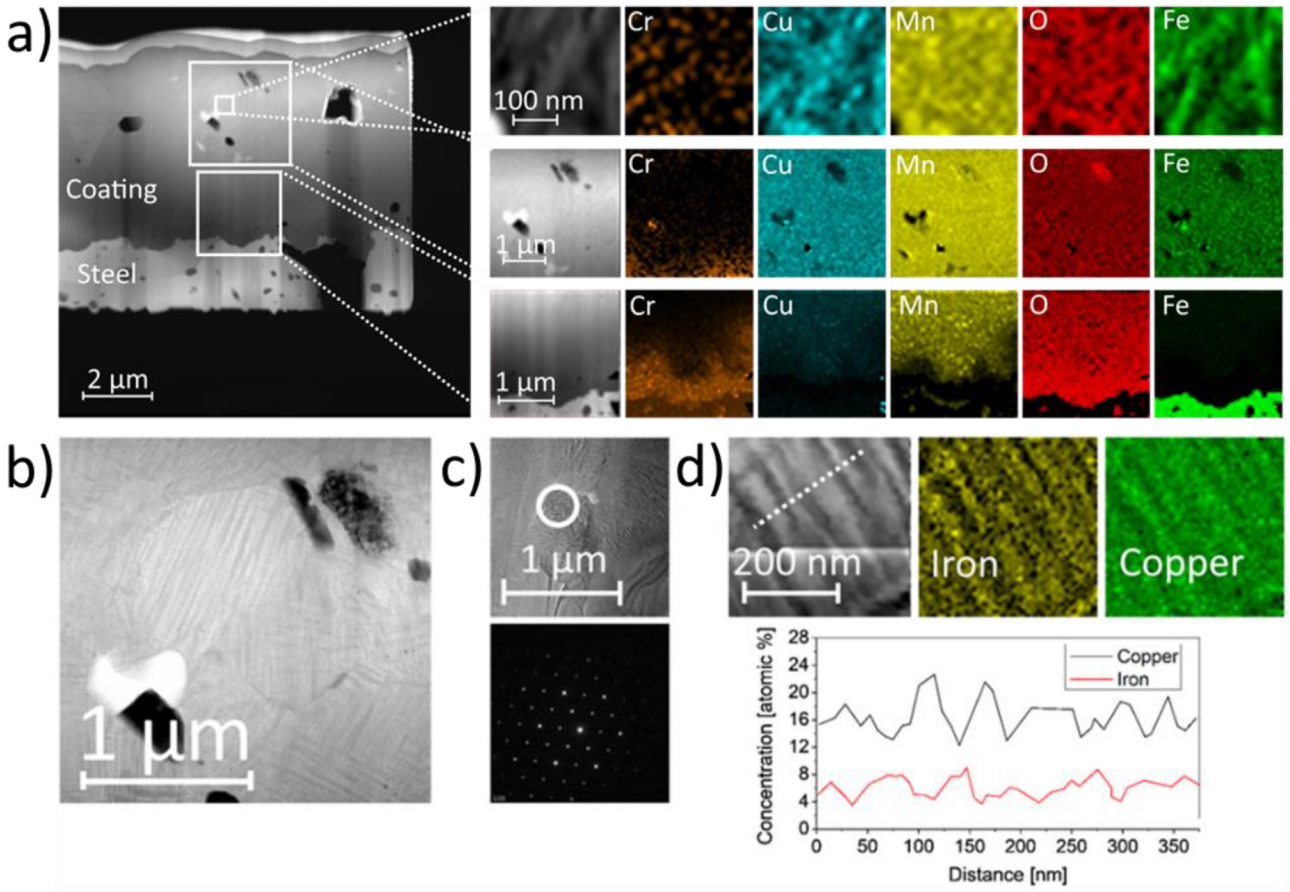

Fig. 7 – a) STEM image of a TEM lamella obtained by FIB from the MnCuFe03-coated coupon and STEM images and the corresponding element distribution maps for the MnCuFe03-coated Crofer 22 APU after 3000 h of oxidation at 750 °C, b) STEM image showing the needle-like structure, c) STEM image and electron diffraction pattern from the marked area in the image, d) EDX line scan and element distribution maps for Fe and Cu from an area that contains the needle-like structures.

Please cite this article as: Ignaczak J et al., Fe-modified Mn_2CuO_4 spinel oxides: coatings based on abundant elements for solid oxide cell interconnects, International Journal of Hydrogen Energy, https://doi.org/10.1016/j.ijhydene.2023.06.041

sample, a needle like structure and nonhomogeneous cation distribution, there is a presence of second phase and further evaluation is needed.

Synchrotron multimodal chemical imaging with micro-focused X-ray beam

To further characterise the structure and chemical composition of the coated samples, XRD and XRF-contrast microscopy studies were performed. Due to the date of availability of the beam line, it was possible to test the samples before the oxidation process and after 1000 h of the experiment. For the study, a 50 μm lamella was cut for 2D scanning imaging. Based on the acquired data, 2D images illustrating the distribution of crystalline phases and chemical composition were generated. 1D profiles of the crystalline phases and elemental distribution were evaluated as a function of the distance from the surface by integrating the 2D images along the dimension parallel to the coating, which resulted in significantly improved statistics which made it possible to analyse the diffraction patterns.

The data presented in Figs. 8 and 9 show the analysis of the XRF measurements for the MnCuFe0 and MnCuFe03 before oxidation test (t = 0 h) and after 1000 h of oxidation at 750 °C (4 samples overall). For reference, SEM/EDX data of similar samples are included in Fig. 8a and d, and 9a and 9d for MnCuFe0 and MnCuFe03, respectively.

For the coating without the addition of iron, the highest concentration of chromium is at the interface between the Crofer 22 APU substrate and the deposited coating. The thickness of the chromia scale is about 1.5 μm and the amount of chromium decreases with the distance from the steel. For comparison, the thickness of the corrosion product observed in the SEM images is below 1 μm and the thickness calculated from the mass gain is 2.4 μm. It can also be observed that the amount of iron is higher near to the steel surface than in the volume of the coating. The concentration of manganese and copper is homogenous and declines near the surface of the substrate in favour of iron and chromium.

The results of the same analysis performed for the MnCuFe0 sample after 1000 h of oxidation at 750 °C are presented in Fig. 8e. It should be noted that the coating on this sample is thinner, at only 7 μm. The thickness of the corrosion product is comparable to that observed on the sample before the oxidation test. Chromium is present in the spinel coating, and it can be observed that there is a thick reaction layer between the chromium and the coating, while beyond this layer, the chromium content is low, at the level of iron, which is in agreement with the EDX line scan performed for the MnCuFe0 sample after 1000 h (Fig. 8d) of oxidation. Based on the XRF and EDX analyses performed for the MnCuFe0 sample after 1000 h of oxidation testing, a thick reaction layer is present between the chromia scale and the coating (Fig. 8d and e). Above this layer, the chromium content is at a low level, comparable to the iron content.

The manganese and copper distribution is no longer homogenous, with their content varying over the distance from the steel surface. Fig. 8c and f illustrate the results of the micro XRD analysis performed on the same lamella as the XRF results. These results are complementary and provide

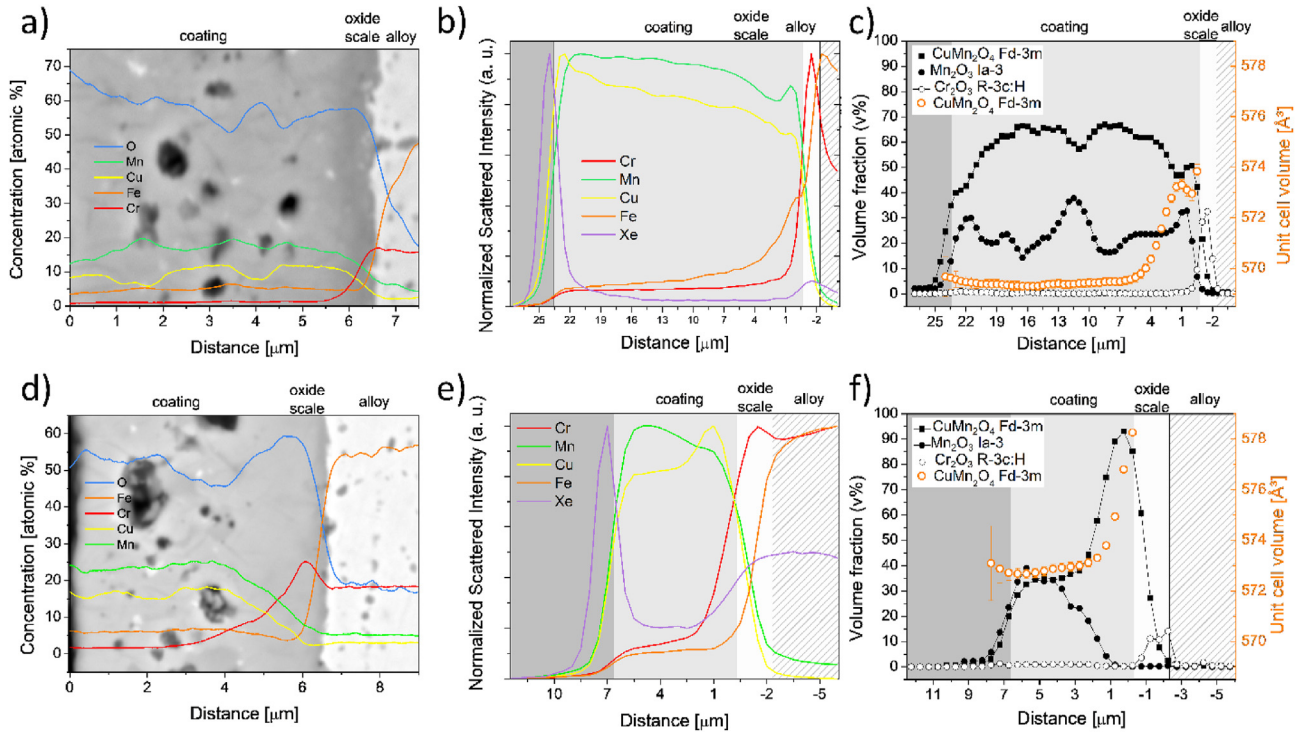

Fig. 8 – Characterisation of MnCuFe0 sample before oxidation a), b), c) and after 1000 h of oxidation test d), e), f); a), d) EDX line scan performed in the whole depth of the coating/substrate system, b), e) XRF analysis performed on the lamella prepared by FIB, c), f) micro XRD analysis performed on lamella prepared by FIB.

Please cite this article as: Ignaczak J et al., Fe-modified Mn_2CuO_4 spinel oxides: coatings based on abundant elements for solid oxide cell interconnects, International Journal of Hydrogen Energy, https://doi.org/10.1016/j.ijhydene.2023.06.041

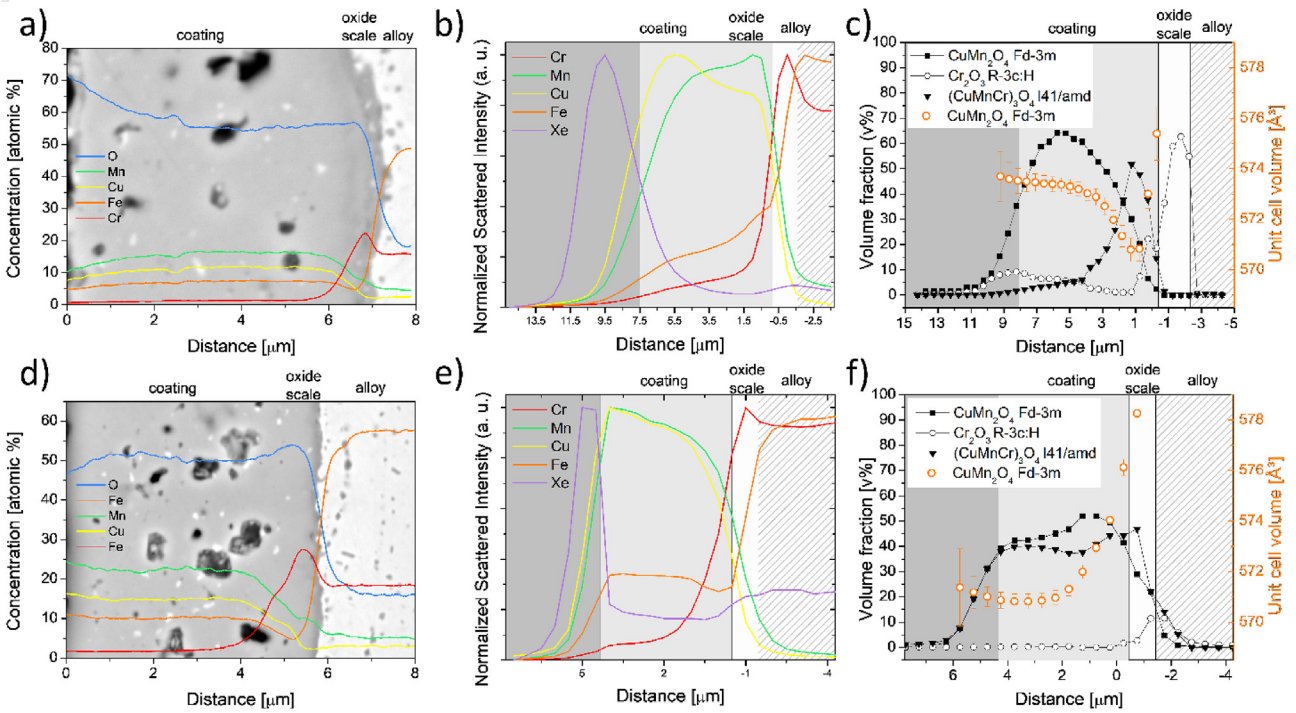

Fig. 9 – Characterisation of MnCuFe03 sample before oxidation a), b), c) and after 1000 h of oxidation test d), e), f); a), d) EDX line scan performed in the whole depth of the coating/substrate system, b), e) XRF analysis performed on the lamella prepared by FIB, c), f) micro XRD analysis performed on lamella prepared by FIB.

information that cannot be obtained otherwise. The MnCuFe0 sample at t = 0 h consists of two phases distributed in the whole volume of the coating, a spinel cubic phase with the Fd-3m space group, and cubic Mn_2O_3 with an Ia-3 space group, as determined from the XRD analysis performed using a standard X-ray diffractometer. The lattice parameters were calculated for the cubic spinel phase and are presented in the figures as a function of the distance from the steel substrate (marked with orange circles). These values increase with the increasing proximity to the substrate and with the higher chromium content. For the sample before oxidation, the unit cell volume for the regular Fd-3m phase (Mn_2CuO_4) in the actual coating layer was calculated as 571 Å^3. In the reaction layer, an increase to 578 Å^3 was observed. An increase in the unit volume cell confirms that the spinel oxide from the coating reacts with the chromium from the substrate material, since chromium has a bigger ionic radii than copper and manganese, and its presence in the cell lattice leads to bigger values of the lattice parameter. The manganese oxide phase is closer to the surface of the coating (top part) and the spinel layer is closer to the substrate, as shown in Fig. 8f.

In Fig. 9, we have presented an analogical result to those described above for the MnCuFe03 sample at t = 0 h and t = 1000 h. The MnCuFe03 coating at t = 0 h before the corrosion test consists of two phases, with one of them corresponding to a regular spinel phase with space group Fd-3m, and the other to tetragonal spinel with space group $I4_1/amd$. These phases are unevenly distributed in the cross-section of the coating, as shown in Fig. 9c. By comparing the XRD and XRF results, it can be seen that one phase contains more manganese and the other one more copper. The chromium oxide formed on the surface of the sample has a thickness of 1 μm. The volume cell parameter for one of the cubic spinel phases near to the top surface is 573 Å^3, while this value drops to 571 Å^3 in the area of the sample where there is more tetragonal spinel phase with a different stoichiometry and then increases near the surface of the steel up to 576 Å^3.

Analysis of the sample after 1000 h of oxidation demonstrates that the coating consists of two phases, one tetragonal symmetry with space group *I41/amd*, and the second one a cubic spinel phase with space group Fd-3m. The distribution of these phases is uniform throughout the volume of the sample. The distribution of all elements in the coating is also uniform, which makes this sample different from the one before oxidation, where copper, manganese, and iron had their maxima and minima. The thickness of the corrosion product calculated from the XRF and XRD data shows that it is about 1 μm, however, it is necessary to take into account that 1 μm is the limit resolution for the technique here (limited by the beam size used here of 1 μm), meaning that this layer is highly likely to be thinner than this. Chromium is present in the coating, forming the reaction layer with a thickness of around 2 μm, but on the surface, its amount decreases significantly. The presented test's results confirm the presence of a second phase in the MnCuFe03 coating, which was also demonstrated by TEM tests on the MnCuFe03 sample after 3000 h of oxidation (Fig. 7), where no uniform Fe and Cu cation distributions were observed. It is worth mentioning that the EDX analysis performed on the MnCuFe03 sample after 1000 h (Fig. 9d) did not detect the presence of a second phase, but the EDX resolution was insufficient to observe the needle-like structure of the material. The lattice volume

Please cite this article as: Ignaczak J et al., Fe-modified Mn_2CuO_4 spinel oxides: coatings based on abundant elements for solid oxide cell interconnects, International Journal of Hydrogen Energy, https://doi.org/10.1016/j.ijhydene.2023.06.041

parameter calculated for this sample equals 571 Å^3 on top surface of the obtained coating, while as it approaches the surface of the steel, this parameter increases up to 578 Å^3 right next to the chromium oxide scale.

Comparing the unit cell volume before and after 1000 h of the experiment, it is worth noting that the values calculated for the regular spinel phase increased with time. This change is probably connected with the reaction of the coating with chromium; this element exhibits the strongest preference to the octahedral position among all transition metal and its ionic radius for Cr^{3+} in the octahedral position is 0.615 Å, and is higher than for manganese, copper or iron, which clearly confirms that the reaction of any of the synthetised spinels with chromium evaporating from the steel surface results in an increase of the unit cell parameter even if we are not able to determine the exact position of the elements in the structure.

Electrical conductivity test-ASR measurement

Fig. 10 shows the Area Specific Resistance (ASR) data recorded during 3000 h of cycling oxidation of the prepared samples. The samples were evaluated after 0 h (as-prepared), 250 h, 1000 h and finally after 3000 h of oxidation at 750 °C. Figs. 10a and b presents the Arrhenius dependence of the area specific resistance, measured in air in a temperature range of 300–750 °C for the investigated samples before oxidation (Fig. 10a) and after 3000 h of oxidation (Fig. 10b).

Consistent with the previously reported conductivity results for the used materials, the ASR measurement for the $Mn_{2-x}CuFe_xO_4$ coating series show lower values (3–5 mΩ cm^{-2} at 750 °C) than the manganese-cobalt spinel (7 mΩ cm^{-2} at 750 °C) and the preox sample (7.5 mΩ cm^{-2} at 750 °C) subjected to analogous oxidation as the coated alloy. The lowest ASR values below 1 mΩ cm^{-2} at 750 °C are measured for steel without any previous heat treatment, which is described in this paper as a reference sample. Among the coated samples, the MnCuFe coating shows promising performance. Application of this material results in a slowed-down ASR increase. For MnCuFe0, the measured values increase from 2.5 mΩ cm^{-2} to 5 mΩ cm^{-2} after 3000 h of oxidation, which is an impressive result. The ASR increase for reference and preox-reference sample is noticeable; from 0.8 mΩ cm^{-2} at 750 °C and 1.2 mΩ cm^{-2} at 500 °C to 30 mΩ cm^{-2} and 50 mΩ cm^{-2} for the

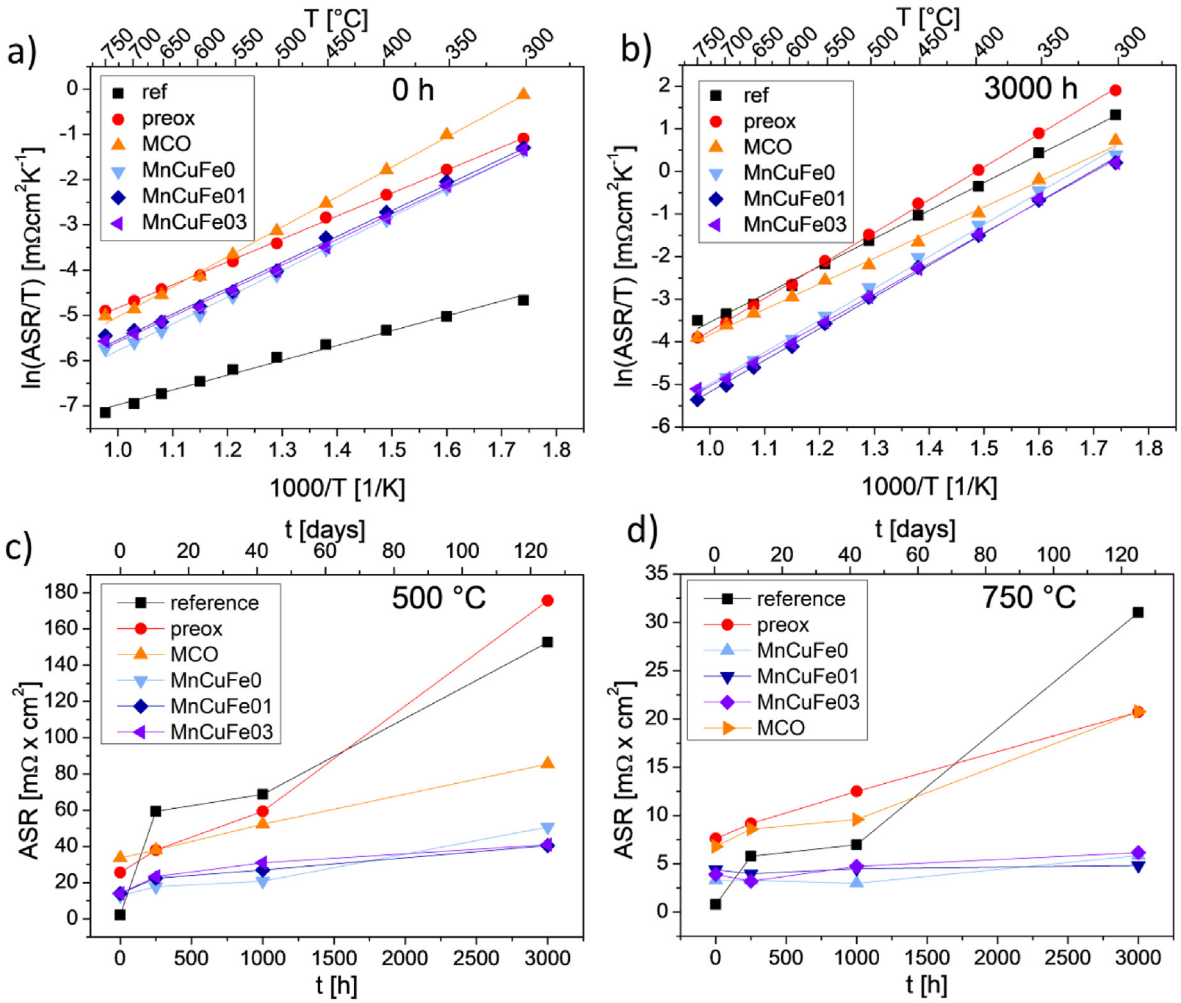

Fig. 10 – Area specific resistant measurement a), b) temperature dependence of ASR for prepared coating before oxidation process and after 3000 h of oxidation test, respectively, c), d) change in ASR values as a function of time at 500 °C and 750 °C, respectively.

Please cite this article as: Ignaczak J et al., Fe-modified Mn_2CuO_4 spinel oxides: coatings based on abundant elements for solid oxide cell interconnects, International Journal of Hydrogen Energy, https://doi.org/10.1016/j.ijhydene.2023.06.041

reference sample, and from 8 mΩ cm^{-2} at 750 °C and 28 mΩ cm^{-2} at 500 °C to 20 mΩ cm^{-2} at 750 °C and 180 mΩ cm^{-2} at 500 °C for the preox-reference sample.

These differences may be due to two phenomena, the first of which is a significantly higher conductivity of MnCuFe spinel than MCO spinel. A second phenomenon that may affect the lower ASR values for MnCuFe spinels is that these materials effectively slow down the formation of chromium oxide; a thinner chromium oxide layer results in a lower contact resistance value.

The resistance of chromium oxide, which mainly forms corrosion products, is several orders of magnitude higher than that of the oxides used for coatings. Liu et al. [51] measured the conductivity of a spinel oxide with the general formula $Mn_{1.5-0.5x}Co_{1.5-0.5x}Cr_xO_4$, x=(0–2) at 800 °C, and found that the values decreased from 60 S cm^{-1} to 0.007 S cm^{-1} as x (chromium content) increases from 0 to 2. No experiments specific to the $(Mn,Cu,Fe,Cr)_3O_4$ oxide have been conducted. However, based on the electrical measurements obtained, it can be concluded that chromium reacts more rapidly with the coating but does not significantly affect the conductivity of the Mn–Cu–Fe-based oxide.

Consistent with Talic et al. [52], the ASR of the system substrate-corrosion product-coating does not depend on the thickness and conductivity of the coating. Similar conclusions were determined by Goebel et al. [53]. However, our work, which directly studied MCO and MnCuFex coatings in similar conditions, shows that the application of higher conductivity coatings can be beneficial in terms of lower ASR, and thus MnCuFex is very promising for practical applications.

Conclusions

In this study, the modified Pechini method was used to synthesise powders with the following stoichiometries: $Mn_{2-x}CuFe_xO_4$ where x = 0, 0.1, 0.3, and $MnCo_2O_4$. The resulting powders were analysed to determine the phase composition, TEC, sintering properties and deposited on ferritic stainless steel (FSS) coupons. All powders were successfully deposited by electrophoretic deposition (EPD) on Crofer 22 APU coupons and sintered in a two-step process, which resulted in a dense and adhesive coating. The prepared samples were oxidised in air at 750 °C for 3000 h, characterised before and after oxidation treatment and compared to the state-of-the-art MCO spinel. It was found that replacing cobalt with copper significantly alters the properties of the oxides. The conductivity of a Mn–Cu–Fe mixed oxide is approximately 20 S cm^{-1} and 40 S cm^{-1} higher at 800 °C and 600 °C, respectively, than the conductivity of an MCO spinel. The results of a dilatometric investigation show that the TEC is decreased to values that match the thermal expansion of the substrate alloy, and that the sintering onset temperature is decreased for the innovative materials. All these properties are beneficial in terms of the application of those materials as a protective coating on FSS in an IT-SOFC.

1. The coatings were densified by a two-step sintering procedure involving 10 h at 1000 °C in H_2 followed by 2 h of oxidation in air at 800 °C, resulting in a coating with good adhesion and no open porosity.
2. The phase composition of the Mn–Cu–Fe coating is affected by the two-step sintering process. High-temperature treatment leads to the formation of a single-phase coating for oxides containing iron: $Mn_{1.9}CuFe_{0.1}O_4$ (MnCuFe01) and $Mn_{1.7}CuFe_{0.3}O_4$ (MnCuFe03).
3. Application of a Mn–Cu–Fe protective coating reduces the parabolic rate constant of Crofer 22 APU at 750 °C by a factor of five, while the state-of-the-art MCO coating reduces the parabolic rate constant by 50 times compared to the uncoated steel.
4. The calculated oxide scale thicknesses of MnCuFe0 and MnCuFe03 are 2.43 μm and 2.18 μm, respectively. These values differ significantly from the thickness of the chromia scale (about 1 μm) observed in SEM and STEM images, and when combined with micro XRD analysis, indicate that chromium reacts with the spinel phase and forms a $(MnCuFeCr)_3O_4$ spinel.
5. Despite their low ability to reduce oxidation kinetics, MnCuFe coatings exhibit a low increase in ASR values during oxidation. For instance, for MnCuFe03 ASR, a gain of ~1 mΩ was observed after 3000 h of exposure at 750 °C. The addition of iron does not appear to affect the electrical properties of the coatings. During the entire investigated oxidation time, the ASR for the MnCuFe0 sample likewise increased by ~1 mΩ.
6. A sufficiently high addition of iron to the Mn–Cu system prevents the formation of manganese oxide Mn_2O_3, however the $Mn_{1.7}CuFe_{0.3}O_4$ (MnCuFe03) sample also contains a second, tetragonal phase.

Declaration of competing interest

The authors declare that they have no known competing financial interests or personal relationships that could have appeared to influence the work reported in this paper.

Acknowledgments

This work is supported by National Science Centre Harmonia 9 project number UMO-2017/26/M/ST8/00438: “Quest for novel materials for solid oxide cell interconnect coatings”. The TEM measurement and analysis have been financed by the project from the European Union’s Horizon 2020 research and innovation program under grant agreement No 823717 and it was performed by the Chalmers Material Analysis Laboratory, CMAL – ESTEEM3. The authors would like to acknowledge the Paul Scherrer Institute, Villigen, Switzerland for access to beamtime at the microXAS beamline of the Swiss Light Source.

Appendix A. Supplementary data

Supplementary data to this article can be found online at https://doi.org/10.1016/j.ijhydene.2023.06.041.

REFERENCES

[1] Sakai N, Horita T, Xiong YP, Yamaji K, Kishimoto H, Brito ME, et al. Structure and transport property of manganese-chromium-iron oxide as a main compound in oxide scales of alloy interconnects for SOFCs. Solid State Ionics 2005;176:681–6. https://doi.org/10.1016/j.ssi.2004.11.012.
[2] Kadowaki T, Shiomitsu T, Matsuda E, Nakagawa H, Tsuneizumi H, Maruyama T. Applicability of heat resisting alloys to the separator of planar type solid oxide fuel cell. Solid State Ionics 1993;67:65–9. https://doi.org/10.1016/0167-2738(93)90310-Y.
[3] Park BK, Lee JW, Lee SB, Lim TH, Park SJ, Park CO, et al. Cu- and Ni-doped Mn1.5Co1.5O4 spinel coatings on metallic interconnects for solid oxide fuel cells. Int J Hydrogen Energy 2013. https://doi.org/10.1016/j.ijhydene.2013.07.025.
[4] Zhu JH, Lewis MJ, Du SW, Li YT. CeO2-doped (Co,Mn)3O4 coatings for protecting solid oxide fuel cell interconnect alloys. Thin Solid Films 2015;596:179–84. https://doi.org/10.1016/j.tsf.2015.07.085. Elsevier.
[5] Hosseini N, Abbasi MH, Karimzadeh F, Choi GM. Development of Cu1.3Mn1.7O4 spinel coating on ferritic stainless steel for solid oxide fuel cell interconnects. J Power Sources 2015;273:1073–83. https://doi.org/10.1016/J.JPOWSOUR.2014.10.017.
[6] Joshi S, Petric A. Nickel substituted CuMn2O4 spinel coatings for solid oxide fuel cell interconnects. Int J Hydrogen Energy 2017;42:5584–9. https://doi.org/10.1016/J.IJHYDENE.2016.08.075.
[7] Wang R, Sun Z, Pal UB, Gopalan S, Basu SN. Mitigation of chromium poisoning of cathodes in solid oxide fuel cells employing CuMn1.8O4 spinel coating on metallic interconnect. J Power Sources 2018;376:100–10. https://doi.org/10.1016/J.JPOWSOUR.2017.11.069.
[8] Ranjbar-Nouri Z, Soltanieh M, Rastegari S. Applying the protective CuMn2O4 spinel coating on AISI-430 ferritic stainless steel used as solid oxide fuel cell interconnects. Surf Coating Technol 2018;334:365–72. https://doi.org/10.1016/J.SURFCOAT.2017.11.036.
[9] Sun Z, Wang R, Nikiforov AY, Gopalan S, Pal UB, Basu SN. CuMn1.8O4 protective coatings on metallic interconnects for prevention of Cr-poisoning in solid oxide fuel cells. J Power Sources 2018;378:125–33. https://doi.org/10.1016/J.JPOWSOUR.2017.12.031.
[10] Waluyo NS, Park SS, Song RH, Lee SB, Lim TH, Hong JE, et al. Protective coating based on manganese–copper oxide for solid oxide fuel cell interconnects: Plasma spray coating and performance evaluation. Ceram Int 2018;44:11576–81. https://doi.org/10.1016/J.CERAMINT.2018.03.220.
[11] Sun Z, Gopalan S, Pal UB, Basu SN. Cu1.3Mn1.7O4 spinel coatings deposited by electrophoretic deposition on Crofer 22 APU substrates for solid oxide fuel cell applications. Surf Coating Technol 2017;323:49–57. https://doi.org/10.1016/j.surfcoat.2016.09.028.
[12] Huang W, Gopalan S, Pal UB, Basu SN. Evaluation of electrophoretically deposited CuMn[sub 1.8]O[sub 4] spinel coatings on crofer 22 APU for solid oxide fuel cell interconnects. J Electrochem Soc 2008. https://doi.org/10.1149/1.2975367.
[13] Ignaczak J, Naumovich Y, Górnicka K, Jamroz J, Wróbel W, Karczewski J, et al. Preparation and characterisation of iron substituted Mn1.7Cu1.3-xFexO4 spinel oxides (x = 0, 0.1, 0.3, 0.5). J Eur Ceram Soc 2020;40:5920–9. https://doi.org/10.1016/j.jeurceramsoc.2020.07.001.
[14] Ranjbar-Nouri Z, Soltanieh M, Rastegari S. Applying the protective CuMn2O4 spinel coating on AISI-430 ferritic stainless steel used as solid oxide fuel cell interconnects. Surf Coating Technol 2018;334:365–72. https://doi.org/10.1016/j.surfcoat.2017.11.036.
[15] Geng S, Zhao Q, Li Y, Mu J, Chen G, Wang F, et al. Sputtered MnCu metallic coating on ferritic stainless steel for solid oxide fuel cell interconnects application. Int J Hydrogen Energy 2017;42:10298–307. https://doi.org/10.1016/j.ijhydene.2017.01.178.
[16] Cu1.3Mn1.7O4 spinel coatings deposited by electrophoretic deposition on Crofer 22 APU substrates for solid oxide fuel cell applications. Elsevier Enhanced Reader n.d, https://reader.elsevier.com/reader/sd/pii/S0257897216308994?token=5D1DFB4A8157BE307E2E013FFE878B5A9EDA836C86D3F1D969A3F3F9666AA1C78E98565BD147752B2E6250CC9F93E70E. [Accessed 14 May 2020].
[17] Huang W, Gopalan S, Pal UB, Basu SN. Evaluation of electrophoretically deposited CuMn[sub 1.8]O[sub 4] spinel coatings on crofer 22 APU for solid oxide fuel cell interconnects. J Electrochem Soc 2008;155:B1161. https://doi.org/10.1149/1.2975367.
[18] Protective coating based on manganese–copper oxide for solid oxide fuel cell interconnects_ Plasma spray coating and performance evaluation | Elsevier Enhanced Reader n.d. https://reader.elsevier.com/reader/sd/pii/S0272884218307995?token=C0D581160AE37FFB4409A848A656776330386302E00BEA885D924AD9B3A14D8B05DEBC4D82B9508CCCE024F2636748F3 (accessed May 14, 2020).
[19] Geng S, Pan Y, Chen G, Wang F. CuFe 2 O 4 protective and electrically conductive coating thermally converted from sputtered CuFe alloy layer on SUS 430 stainless steel interconnect. Int J Hydrogen Energy 2019;44:9400–7. https://doi.org/10.1016/j.ijhydene.2019.02.117.
[20] Grolig JG, Alnegren P, Froitzheim J, Svensson JE. Copper iron conversion coating for solid oxide fuel cell interconnects. J Power Sources 2015;297:534–9. https://doi.org/10.1016/j.jpowsour.2015.06.139.
[21] Zhang W, Hua B, Duan N, Pu J, Chi B, Li J. Cu-Fe spinel coating as oxidation barrier for Fe-16Cr metallic interconnect in solid oxide fuel cells. J Electrochem Soc 2012;159:C388–92. https://doi.org/10.1149/2.021209jes.
[22] Hosseini SN, Karimzadeh F, Enayati MH, Sammes NM. Oxidation and electrical behavior of CuFe2O4 spinel coated Crofer 22 APU stainless steel for SOFC interconnect application. Solid State Ionics 2016;289:95–105. https://doi.org/10.1016/j.ssi.2016.02.015.
[23] Hosseini N, Abbasi MH, Karimzadeh F, Choi GM. Development of Cu1.3Mn1.7O4 spinel coating on ferritic stainless steel for solid oxide fuel cell interconnects. J Power Sources 2015;273:1073–83. https://doi.org/10.1016/j.jpowsour.2014.10.017.
[24] Sun Z, Wang R, Nikiforov AY, Gopalan S, Pal UB, Basu SN. CuMn1.8O4 protective coatings on metallic interconnects for prevention of Cr-poisoning in solid oxide fuel cells. J Power Sources 2018;378:125–33. https://doi.org/10.1016/j.jpowsour.2017.12.031.
[25] Zhu Z, Darl-Uzu C, Pal U, Gopalan S, Hussain AM, Dale N, et al. Comparison of Cu–Mn and Mn–Co spinel coatings for solid oxide fuel cell interconnects. Int J Hydrogen Energy 2022. https://doi.org/10.1016/J.IJHYDENE.2022.08.239.
[26] Oh SU, Kim D, Lee IT, Choi CS, Lee JA, Heo YW, et al. Electrophoretic deposition and low-temperature densification of Cu1.35Mn1.65O4 spinel for an interconnect protective coating in solid oxide fuel cells. Int J Hydrogen Energy 2022;47:33410–9. https://doi.org/10.1016/J.IJHYDENE.2022.07.259.
[27] Danks AE, Hall SR, Schnepp Z. The evolution of "sol-gel" chemistry as a technique for materials synthesis, vol. 3; 2016. p. 91. https://doi.org/10.1039/c5mh00260e.
[28] Sanjabi S, Obeydavi A. Synthesis and characterization of nanocrystalline MgAl2O4 spinel via modified sol–gel

Please cite this article as: Ignaczak J et al., Fe-modified Mn_2CuO_4 spinel oxides: coatings based on abundant elements for solid oxide cell interconnects, International Journal of Hydrogen Energy, https://doi.org/10.1016/j.ijhydene.2023.06.041

method. J Alloys Compd 2015;645:535–40. https://doi.org/10.1016/J.JALLCOM.2015.05.107.
[29] Landauer R. Electrical conductivity in inhomogeneous media. AIP Conf Proc 2008;40:2. https://doi.org/10.1063/1.31150.
[30] Schneider CA, Rasband WS, Eliceiri KW. NIH Image to ImageJ: 25 years of image analysis. Nat Methods 2012 97 2012;9:671–5. https://doi.org/10.1038/nmeth.2089.
[31] Staniskowski M, Hilpert K, Markus T, Singheiser L, Wessel E. Chromium vaporization from high temperature alloys, I. Chromia-forming steels and the influence of outer oxide layers. J Electrochem Soc 2007;154:A295–306. https://doi.org/10.1149/1.2434690.
[32] Yang Z, Xia G, Simner SP, Stevenson JW. Thermal growth and performance of manganese cobaltite spinel protection layers on ferritic stainless steel SOFC interconnects. J Electrochem Soc 2005;152:A1896. https://doi.org/10.1149/1.1990462/XML.
[33] Bobruk M, Molin S, Chen M, Brylewski T, Hendriksen PV. Sintering of MnCo2O4coatings prepared by electrophoretic deposition. Mater Lett 2018. https://doi.org/10.1016/j.matlet.2017.12.046.
[34] Fast Azimuthal Integration using Python — pyFAI 0.22.0a10 documentation. n.d, https://pyfai.readthedocs.io/en/master/. [Accessed 12 October 2022].
[35] PyMca Home nd. https://pymca.sourceforge.net/index.html. [Accessed 12 October 2022].
[36] Danks AE, Hall SR, Schnepp Z. The evolution of "sol-gel" chemistry as a technique for materials synthesis. Mater Horizons 2016;3:91. https://doi.org/10.1039/c5mh00260e.
[37] Afriani F, Hermanto B, Sudiro T. Synthesis of CuMn 2 O 4 spinel and its magnetic properties characterization. AIP Conf Proc 1964;2018:020016. https://doi.org/10.1063/1.5038298.
[38] Petric A, Ling H. Electrical conductivity and thermal expansion of spinels at elevated temperatures. J Am Ceram Soc 2007;90:1515–20. https://doi.org/10.1111/J.1551-2916.2007.01522.X.
[39] Talic B, Hendriksen PV, Wiik K, Lein HL. Thermal expansion and electrical conductivity of Fe and Cu doped MnCo2O4 spinel. Solid State Ionics 2018. https://doi.org/10.1016/j.ssi.2018.09.018.
[40] Smeacetto F, Salvo M, Ferraris M, Cho J, Boccaccini AR. Glass-ceramic seal to join Crofer 22 APU alloy to YSZ ceramic in planar SOFCs. J Eur Ceram Soc 2008;28:61–8. https://doi.org/10.1016/j.jeurceramsoc.2007.05.006.
[41] Sinha APB, Sanjana NR, Biswas AB, Iucr. On the structure of some anganites, vol. 10; 1957. p. 439–40. https://doi.org/10.1107/S0365110X57001450. Urn:Issn:0365-110X.
[42] Talic B, Falk-Windisch H, Venkatachalam V, Hendriksen PV, Wiik K, Lein HL. Effect of coating density on oxidation resistance and Cr vaporization from solid oxide fuel cell interconnects. J Power Sources 2017;354:57–67. https://doi.org/10.1016/J.JPOWSOUR.2017.04.023.
[43] Zanchi E, Ignaczak J, Kamecki B, Jasiński P, Molin S, Boccaccini AR, et al. Manganese–cobalt based spinel coatings processed by electrophoretic deposition method: the influence of sintering on degradation issues of solid oxide cell oxygen electrodes at 750 °C. Mater 2021;14:3836. https://doi.org/10.3390/MA14143836. 2021;14:3836.
[44] Asensio-Jimenez C, Niewolak L, Hattendorf H, Kuhn B, Huczkowski P, Singheiser L, et al. Effect of specimen thickness on the oxidation rate of high chromium ferritic steels: the significance of intrinsic alloy creep strength. Oxid Met 2013;79:15–28. https://doi.org/10.1007/S11085-012-9323-5.
[45] Przybylski K, Brylewski T, Durda E, Gawel R, Kruk A. Oxidation properties of the Crofer 22 APU steel coated with La 0.6Sr0.4Co0.2Fe0.8O3 for IT-SOFC interconnect applications. J Therm Anal Calorim 2014;116:825–34. https://doi.org/10.1007/S10973-013-3594-1.
[46] Mazur Ł, Molin S, Dąbek Jarosław, Durczak Karol, Pyzalski M, Tomasz Brylewski. Physicochemical properties of Mn 1.45 Co 1.45 Cu 0.1 O 4 spinel coating deposited on the Crofer 22 H ferritic steel and exposed to high-temperature oxidation under thermal cycling conditions, vol. 147; 2022. p. 5649–66. https://doi.org/10.1007/s10973-021-10884-2.
[47] Falk-Windisch H, Svensson JE, Froitzheim J. The effect of temperature on chromium vaporization and oxide scale growth on interconnect steels for Solid Oxide Fuel Cells. J Power Sources 2015. https://doi.org/10.1016/j.jpowsour.2015.04.040.
[48] Sachitanand R, Sattari M, Svensson JE, Froitzheim J. Evaluation of the oxidation and Cr evaporation properties of selected FeCr alloys used as SOFC interconnects. Int J Hydrogen Energy 2013. https://doi.org/10.1016/j.ijhydene.2013.09.044.
[49] Stanislowski M, Wessel E, Hilpert K, Markus T, Singheiser L. Chromium Vaporization from High-Temperature Alloys, I. Chromia-forming steels and the influence of outer oxide layers. J Electrochem Soc 2007;154:A295. https://doi.org/10.1149/1.243469.
[50] Talic B, Molin S, Hendriksen PV, Lein HL. Effect of pre-oxidation on the oxidation resistance of Crofer 22 APU. Corrosion Sci 2018;138:189–99. https://doi.org/10.1016/J.CORSCI.2018.04.016.
[51] Liu Y, Fergus JW, Cruz C Dela. Electrical properties, cation distributions, and thermal expansion of manganese cobalt chromite spinel oxides. J Am Ceram Soc 2013. https://doi.org/10.1111/jace.12254.
[52] Talic B, Molin S, Wiik K, Hendriksen PV, Lein HL. Comparison of iron and copper doped manganese cobalt spinel oxides as protective coatings for solid oxide fuel cell interconnects. J Power Sources 2017. https://doi.org/10.1016/j.jpowsour.2017.10.060.
[53] Goebel C, Fefekos AG, Svensson JE, Froitzheim J. Does the conductivity of interconnect coatings matter for solid oxide fuel cell applications? J Power Sources 2018;383:110–4. https://doi.org/10.1016/j.jpowsour.2018.02.060.

Please cite this article as: Ignaczak J et al., Fe-modified Mn_2CuO_4 spinel oxides: coatings based on abundant elements for solid oxide cell interconnects, International Journal of Hydrogen Energy, https://doi.org/10.1016/j.ijhydene.2023.06.041